THESIS FOR THE DEGREE OF LICENTIATE OF ENGINEERING

Atom Probe Tomography Investigations of Biologically Relevant Nanoparticles

GUSTAV ERIKSSON

Department of Chemistry and Chemical Engineering

CHALMERS UNIVERSITY OF TECHNOLOGY

Gothenburg, Sweden 2022

Atom Probe Tomography Investigations of Biologically Relevant Nanoparticles
GUSTAV ERIKSSON

Department of Chemistry and Chemical Engineering
Chalmers University of Technology
SE-412 96 Gothenburg
Sweden
Telephone + 46 (0)31-772 1000

Cover:
Top left: TEM micrograph of a gold nanoparticle. Scale bar: 2 nm.
Top right: APT reconstruction of a part of a gold nanoparticle with its silver content highlighted. Scale bar: 2 nm.
Bottom left: TEM micrograph of chromium embedded hydroxyapatite nanoparticles on a titanium surface. Scale bar: 10 nm.
Bottom right: Sub-volume of an APT reconstruction through the hydroxyapatite nanoparticle-titanium interfaces, with calcium, phosphorous and carbon in the titanium surface oxide highlighted. Scale bar: 5 nm.

Atom Probe Tomography Investigations of Biologically Relevant Nanoparticles
GUSTAV ERIKSSON
Department of Chemistry and Chemical Engineering
Chalmers University of Technology

Abstract

The study of materials at the nanoscale is essential in many scientific disciplines. For example, in materials science the size of the building blocks of a material is directly linked to its properties. New materials are constantly being developed having features at the nanoscale, for example nanoparticles that are used in fields such as catalysis, electronics, and medicine. In biology, many features exist which have nanosized structures including proteins. The 3D secondary structure of proteins is directly linked to their functions; hence structure determination of proteins is of high interest to gain information of biological processes that serves the development of future medicines.

Due to the importance of nanostructures, many methods for their investigation have been developed such as X-ray diffraction, electron microscopy, and atom probe tomography. These methods rely on different probes and are thus often considered complementary as they provide different information. For the same reason, they put different constraints or limitations on the materials studied.

In this work, two novel methods for studying nanoparticles of biological relevance, gold nanoparticles and hydroxyapatite nanoparticles, have been developed for analysis using atom probe tomography.

Gold nanoparticles are popularly used as markers for biomolecules and to immobilize biomolecules on surfaces with retained function and activity. Several methods have been developed in the last decade to study nanoparticles using atom probe tomography, generally involving forming a metal matrix embedding the particles in a material from which a specimen can be made. In this thesis, an alternative approach utilizing a silica matrix made by a sol-gel method used to embed a gold nanoparticle covered surface is presented. This silica-based method provides an environment for the particles that is similar to an aqueous environment.

Nanoparticles of hydroxyapatite, a mineral that is found in bone and teeth, are commonly used as biomaterials, for example as coatings to improve the performance of surgical implants. In this thesis, hydroxyapatite nanoparticles immobilized onto titanium are examined. The analysed surfaces were sputter coated with chromium, forming a matrix that allows for correlative transmission electron microscopy and atom probe tomography analysis. It is shown that calcium and phosphorous integrated into the surface oxide of the titanium, revealing detailed insights on immobilization of the nanoparticles on the surface. This integration resembles the osseointegration of bone when compared to similar titanium implants being introduced to the human body.

Keywords: Nanoparticles; surface modification; ligands; silica; electron microscopy; atom probe tomography; hydroxyapatite; titanium.

List of publications

Paper 1.

Silica Embedded Gold Nanoparticles Analysed by Atom Probe Tomography

Gustav Eriksson, Mats Hulander, Mattias Thuvander, Martin Andersson

Manuscript

Paper 2.

4D Atomically Resolved Interfacial Analysis of Bone-like Hydroxyapatite Nanoparticles and Titanium

Gustav Eriksson, Mats Hulander, Mattias Thuvander, Martin Andersson

Manuscript

Contribution report

Paper 1. Main author. Performed synthesis, sample preparation, analyses, data evaluation and wrote the first draft of the manuscript.

Paper 2. Main author. Performed transmission electron microscopy (TEM) and atom probe tomography (APT) sample preparation, TEM and APT analysis, data evaluation and wrote the first draft of the manuscript.

Table of Contents

1. Introduction

1.1. Background

In our everyday lives, we experience and understand ourselves and the world at the macroscale. We see our bodies and the surrounding world at this scale and understand how they function at this level. However, in our efforts to reach a deeper understanding of how we and our world work we realise that many of the phenomena that makes life possible occurs at much smaller scale, even at the molecular level. This becomes especially apparent when we turn unwell in one way or another and need to understand how to treat this in an effective manner. All living organisms are built up and regulated by molecules that together form macroscopical structures having specified functions. The most diverse class of such molecules are proteins as they are responsible for carrying out most of the essential functions in living organisms. The chemical composition of proteins can routinely be found as it is provided by their blueprint in our genome (DNA), however, their function is highly dependent on their folding into 3D structures and this information requires other methods to be obtained. While methods such as X-ray diffraction (XRD), nuclear magnetic resonance (NMR) and cryo-electron microscopy (cryo-EM) have provided great insight in the 3D structure of proteins, many of them remain elusive. One large class of proteins that are relatively unstudied are the proteins situated in the cellular membrane, whose structure is of important to understand the mechanisms of viral infections and in drug development (1).

Another example showing that an understanding of mechanisms at small scale is useful is when treating medical conditions using medical devices, such as implants. Surgical implants for joint replacements are commonly made out of titanium and while suitable due to its mechanical properties and biocompatibility, poor integration with bone causes an environment prone to bacterial growth, that may result in infections difficult to treat. A method to improve the integration into bone, referred to as osseointegration, is to functionalize titanium surfaces with hydroxyapatite. Hydroxyapatite is a mineral found in natural bone, which have proven to improve the biocompatibility and speed up the integration process

while retaining the mechanical properties of the underlying titanium. Of special interest for such surface modifications is to use nanostructured hydroxyapatite, since this is the natural occurring form of apatite in bone tissue, hence a biomimetic surface is formed on the implant when coated with these particles. Even though such nanostructured implants are in clinical use, little is known about the mechanism for immobilization of nanostructured hydroxyapatite on a titanium surface and how this compares to the naturally occurring osseointegration of titanium in bone.

In other disciplines of science, an understanding of materials properties at the nanoscale is also of importance and several methods have been developed to provide such information. For metallurgical studies, atom probe tomography (APT) has proven to be a useful method to obtain information about a material's structure at the atomic scale. By field evaporation of individual atoms from a specimen that are collected by a position sensitive mass spectrometric detector, a reconstruction of the analysed specimen can be created with sub-nanometer resolution and equal mass sensitivity across the entire periodic table (2). Development of the instrumentation used, especially the introduction of focused ion beam specimen preparation methods and laser assisted field evaporation has made the technique available to study more materials, including some biological ones (3).

1.2. Scope of the thesis

In this thesis, novel concepts for enabling APT analysis of nanoparticles immobilized on surfaces and potentially allowing for studies of proteins are explored. Previous challenges relating to the study of biological materials using APT are addressed and the proposed methods may allow for high throughput of analysis using conventional methods for specimen preparation, such as focused ion beam-scanning electron microscopy (FIB-SEM) lift-outs. The work builds on a previous study conducted by Sundell *et al.* showing how a silicon dioxide matrix can be formed encapsulating proteins in a material that is possible to analyse using APT. This work proved successful in being able to encapsulate a protein and consequently run as well as reconstruct a sample of it using APT. However, the throughput of the method proved to be insufficient due to the low concentration and uneven distribution of the proteins in the samples (4). This led to a low likelihood of finding a protein in a volume analysed by APT.

To circumvent the challenges of finding the protein in the silica matrix, a novel methodology was investigated in this thesis, where the proteins are attached to a surface prior to silica embedding. This would make the proteins of interest localized to a specific plane in the sample in a controlled manner, allowing for a higher probability of being able to find and study them using APT. Furthermore, it was attempted to bind the proteins to nanoparticles attached to the surface, to reduce the risk of the proteins undergoing structural changes as they adsorb to the surface.

Another system, also of biological interest, that was investigated are titanium substrates coated with hydroxyapatite nanoparticles to be used as an implant material. Such coated titanium was studied with APT to reveal the nature of the nanoparticles binding to the surface oxide of titanium. This analysis provided insight to the mechanism of how the nanostructuring of the surface using synthetic hydroxyapatite can speed up the integration of the implant when compared to the integration of bone in the implant's surface oxide *in vivo*.

2. Theoretical background

In the following chapter, a theoretical background of the studied materials, the methods used for sample preparation as well as the used analytical techniques will be presented.

2.1. Proteins and their relevance

Proteins are one of the main components of all living systems. They are responsible for most of the functions in the cells, such as transport, moving and facilitating (catalysing) chemical reactions (converting one compound into another). While other biological macromolecules including carbohydrates and lipids are quite limited in their variations, proteins come in countless of variations. This high variety of protein structures is the reason for the high number of functions they can carry out in living organisms. Proteins are formed through what is called the central dogma, where genes in the organism's DNA, which contain a certain nucleic acid sequence that act as a blueprint, is translated into a predetermined amino acid sequence (5). The 20 naturally occurring amino acids found in living organisms can be combined into countless variations of proteins, many of which are hundreds of amino acids long. While the sequence can be easily determined by examining the gene coding for a protein, it does not necessarily provide any information about the 3D structure that the protein will have when correctly folded. Herein lies the challenge when studying proteins, as their shape is as important for this function as their amino acid sequence.

Due to the importance of proteins, their shape dependency for their function and the difficulties in predicting shape from chemical structure, characterization methods for proteins have been of importance to understand life at a fundamental level. The first proteins were characterized using X-ray diffraction (6); however, this technique has proven quite limited to study most proteins due to inherent limitations; in order to study proteins using X-ray diffraction, the biomolecules need to be crystallized in larger structures and most of them do not retain their native structure under these conditions. Other techniques that have been used to

characterize proteins are nuclear magnetic resonance (NMR), and cryogenic electron microscopy (cryo-EM), which both have contributed to an increased understanding of the structure of proteins. Such methods also have limitations, for example NMR provides less unambiguous information when the macromolecular proteins become bigger and cryo-EM does not provide any chemical information, disregarding one dimension of the analysis.

2.2. Nanoparticles – synthesis and applications

In recent decades, nanoparticles have been of vast interest. Due to their small size, high surface to volume ratio, nanoparticles display remarkably different properties from the same material in bulk form (7). They are now being applied in various fields such as catalysis, energy conversion, electronics and in biological application, mainly for sensing and transport. Due to their importance in modern industries and life, the studies of nanoparticles have increased and today the synthesis and characterization of them are well explored fields.

There are two main pathways to form nanoparticles, top-down and bottom-up. In the top-down method, larger objects of the material of interest are through various methods subsequentially made smaller until they are in the nanometer size regime. This can be done through mechanical processes such as grinding and by methods such as electron and ion lithography. The bottom-up method consists of synthesizing the particles from even smaller components, such as individual molecules, in a controlled manner to receive nanoparticles of a desired size and shape. A well-known example is the Turkevich method, where a $HAuCl_4$ solution is reduced by citrate in boiling water under stirring (8). The citrate acts as both a reducing agent for the gold salt and as a stabilizer for the nanoparticles formed by the gold ions. This yields nanoparticles with a narrow size distribution that can be controlled by adjusting the citrate and $HAuCl_4$ ratio (9). These particles can then be used as seeds for seed-growth formation of larger nanoparticles with varying shapes by adding a growth solution (10). Such growth solutions often contain the same metal salt together with stabilizing compounds and shape directing agents, which in the case of gold nanoparticles often is silver (11). In the case of silver stabilization of gold particles, the silver has an affinity to certain

facets of the gold crystal structure, which reduces the particle growth rate on them. This makes the nanoparticles grow faster in other directions, promoting the emergence of specific particle shapes.

Nanoparticles can thus have various shapes (12), due to the fact that while the equilibrium shape for liquids always is spheres since the sphere always has the smallest possible surface area for any given volume. But for metals that nanoparticles are made from, the surface energy also is facet dependent, meaning that it depends on the orientation of the crystal and which of its sides that are exposed. Furthermore, features such as defects and edges can have various contributions to the surface energy of a nanoparticle, affecting its shape. The final shape of a nanoparticle is often obtained by twinning of (tetrahedral) subunits to form structures such as truncated octahedra, the shape normally observed in gold nanoparticles.

While metallic nanoparticles consisting of only one element are non-trivial to fully control, the complexity increases when more elements are introduced. There can be several motivations to introduce additional elements to a nanoparticle system. In some cases, a metal has desired properties but is expensive and it can be beneficial to form core-shell particles with a more abundant material in the core. Other times, the addition of another element to the synthesis will give a higher degree of uniformity of the final particles or enable the formation of other particle shapes. In either case, nanoparticle systems consisting of more than one element give new challenges to characterize and fully understand. When studying nanoparticles consisting of one element it is generally enough to learn their size and shape distributions, but when studying particles consisting of more elements it is also important to understand the distribution of the elements inside the particles.

2.2.1. Nanoparticle surface interactions

For many applications, it is desired to modify a surface by covering it with nanoparticles and various protocols have been formulated to achieve a satisfactory particle coverage. Two main methods for nano structuring of a

surface are by electrostatic interactions and by chemisorption. In order to utilize electrostatics to modify a surface with nanoparticles, the surface charge of the nanoparticles needs to be considered and the surface charge of the substrate should be chosen or modified to have the opposite sign. In general, nanoparticles are stabilized by ligands or capping agents that prevent particle aggregation by electrostatic repulsion and when these are positively charged, it is possible to electrostatically modify a negatively charge surface with the nanoparticles.

Chemisorption utilizes covalent bonding of the nanoparticles to immobilize them to a surface. This can be achieved by modifying the substrate surface with a compound that contains a terminating group with high affinity to the nanoparticles of interest and that will be exposed to the surrounding medium. Such a terminating group can be an amino-group or a thiol-group, both which have been used to immobilize inorganic nanoparticle to surfaces (13)(14).

2.2.2. Nanoparticle protein interactions

Inorganic nanoparticles, mainly gold, silica, and iron oxide ones, have been found to have biocompatible properties and therefore have been used in biological applications (15)(16). For this reason, several strategies have been developed to form inorganic nanoparticle-biomolecule complexes (17). One commonly used example of a method to bind biomolecules to inorganic gold nanoparticles is by using thiol linkers, where a thiol end can bind to the nanoparticles with a bond that has a covalent character (18)(19). Another commonly used linker in biotechnology and binding of biomolecules with nanomaterials is the protein streptavidin, due to its ability to bind strongly to biotin (20). This property, in combination with the well-established methods to modify biomolecules with biotin, allows for linking of biomolecules to nanoparticles in creative ways.

### 2.2.3. Biologically relevant nanoparticles

Nanoparticles have been used in a plenitude of biological applications, and in some cases, the nanoparticles themselves are of biological origin or character. For

example, lipid nanoparticles, that are spherical particles made of phospholipids or liposomes, that are vesicles made out of lipid bilayers, *i.e.*, membranes usually made of phospholipids. These types of nanoparticles have been utilized in for example drug delivery, such as in mRNA vaccines (21).

Another example of nanoparticles of biological interest is hydroxyapatite nanoparticles, that are made out of the same material that forms the mineral component in human bone and can be used in biomaterials designed to integrate with bone tissue (22). They have proven useful as a surface coating on implant materials, as they increase the biocompatibility of the implant to the bone (23)(24). This promotes the bone growth onto the implant material, improving osseointegration and by decreasing the time required for proper adhesion the risk for infections by bacterial growth is reduced.

2.3. Silica for biomolecular encapsulation

Silicon dioxide, silica, is the second most abundant mineral in the earth's crust, in form of quartz, and it is the main component of for example sand and glass (25)(26). Silica also has plenty of industrial applications, often in the form of colloidal particles. Despite being inorganic, silica can be found in biological systems, for example in diatoms that are silicified algae. Inspired by this, silica matrixes have also been proven to be a suitable material for biomolecular encapsulation, for increasing both stability and activity of enzymes (27). Silica nanoparticles can be produced synthetically through various methods, out of which one of the most common ones is the Stöber method (28). The Stöber method, is a two-step method where a precursor, often a silicon alkoxide such as tetraethyl orthosilicate, TEOS, is first hydrolysed in the presence of water followed by a condensation polymerization reaction forming the silica. The process can be described by the reaction formulas below.

$$\equiv Si - OR + H_2O \leftrightarrow \equiv Si - OH + ROH$$

$$\equiv Si - OR + OH - Si \equiv \leftrightarrow \equiv Si - O - Si \equiv + ROH$$
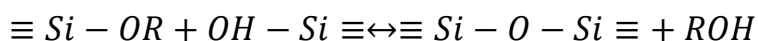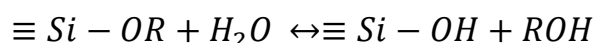
The silanol groups formed in the hydrolysis reaction are quite reactive and will form siloxane bridges that is the backbone of the condensed polymer. As the Stöber process is sensitive to pH, it is often performed under basic conditions for the hydrolysis and the process also leads to the presence of alcohol as a by-product (29). Since this environment often causes denaturation of sensitive biological materials, such as proteins, alternative methods are of interest if they are to be incorporated into the synthesized silica material. One such method utilizes an aqueous solution of sodium silicate salt, also known as water glass, which rapidly gels when the solution pH is adjusted to neutral levels (30)(31)(32). By adding biomolecules such as proteins to a buffered water glass solution, a gel containing the compounds of interest can be obtained. One other method that can be used to adjust the pH level of such sodium silicate solutions is the use of an acidic ion-exchange column, where the sodium ions are replaced with hydrogen. The pH of the silicate solution can then be changed from basic to neutral, increasing the rate of condensation polymerization rapidly. Sol-gels generally forms materials with shapes determined by the shape of the container upon drying, however, thin films can be obtained by either dip- or spin-coating (33).

2.4. Electron microscopy

In traditional optical microscopy, lenses are used to spread photons reflected from features close to each other in an object, thus forming a magnified imaged when observed by an eye or a camera. However, there is a limit as to how small features that can be resolved by an optical microscope, imposed by the wavelength of visible light. Electrons, especially accelerated at the voltage levels used in an electron microscope, have a far shorter wavelength than visible light, making smaller features observable (34). The electrons are exposed to the analysed specimen in form of a beam that is generated from a source, called an electron gun, analogous to the lamp in an optical microscope. The electron beam is then focused on the specimen using electrostatic and electromagnetic lenses, analogous to the glass lenses in the optical microscope. When the electrons interact with the matter in the analysed specimen, several types of scattering events occur that provides different kinds of information that can be sorted in two

10

general categories, scattered electrons, and X-rays. By collecting either scattered electrons or X-rays, information is obtained about the studied sample.

There are two main types of electron microscopes, the scanning electron microscope, SEM and the transmission electron microscope, TEM. They operate at different resolutions and can provide different information about the analysed material, making the choice of method important depending on the questions at hand.

2.4.1.Scanning electron microscopy

To study the surface of bulk materials, the most commonly used electron microscope is the SEM. The electron beam usually has an acceleration voltage of 1-30 kV and is formed into a small spot by the electromagnetic lenses and raster scanned using scanning coils across an area of the specimen surface (35). In each position, the generated electrons are collected by the detector and by measuring the relative number of electrons detected a contrast-based micrograph is formed. By the collection of secondary electrons from the sample, a micrograph containing topographical information is obtained, as edges generates more secondary electrons than flat surfaces. If back-scattered electrons are collected, an atomic number contrast micrograph is obtained, as atoms with a high atomic number has a higher probability to scatter incident electrons. The incident electrons have an interaction volume with the specimen, which defines the region from which the various signals are generated. Secondary electrons are generated in the first few nanometres below the surface, whereas characteristic X-rays can be generated from a volume of up to a micrometre from where the electron beam is focused on the sample. This means that the resolution is dependent on which type of signals that are collected.

2.4.2.Transmission electron microscopy

TEM uses higher energy electrons than SEM, with acceleration voltages usually between 100 and 300 kV, that as the name suggests, are transmitted through the

specimen to provide higher resolution images (34). This introduces the requirement that the specimen needs to be sufficiently thin for the electrons to be able to pass through, which generally means below 100 nm. If the specimen is too thick, the electrons will scatter too many times and consequently not be able to exit the sample along the optical axis. In the ordinary TEM mode, the electron beam is shaped into a broad, parallel beam using the electromagnetic lenses, while in scanning TEM mode, STEM, the beam is converged into a small probe that is raster scanned on the specimen similar as in SEM.

In TEM, the same type of signals is generated as in SEM, meaning secondary electrons, back-scattered electrons, and characteristic X-rays. However, in general the electrons that have been transmitted through the specimen are collected and used for imaging. The transmitted electrons that are scattered at no or small angles are collected by a detector along the optical axis and generally used for bright-field imaging. This sort of imaging can provide phase-contrast information, but Z-contrast, *i.e.*, contrast based on the atomic number of different atoms in the specimen and thickness contrast also occurs. Electrons that are scattered at a higher angle can be used for dark-field imaging and collected using an annular detector around the optical axis and when the acceptance angle is about 50 mrad it is termed high-angle angular dark-field imaging, HAADF. In this mode, a STEM probe is generally used and variations in Z-number in the sample become more accentuated.

2.4.3. Focused ion beam SEM dual beam systems

By combining an SEM instrument with a focused ion beam, FIB, into a FIB-SEM dual beam system, new possibilities for analysis and material manipulation open up (36). The FIB uses ions far heavier than electrons, often Ga^+ but in newer instruments also noble gases, to be accelerated onto the specimen in a well-defined spot similarly to the electron beam. This can be used for imaging, as secondary electrons are generated when the ions interact with the specimen (37), but more importantly for manipulation of the specimen, material is milled away by the ions. By first scanning the ion beam to mill well defined patterns, then the

electron beam can be used to perform cross sectional imaging of a specimen that gives information not revealed by ordinary surface imaging.

An important application of FIB-systems is to utilize the milling capabilities to prepare specimen for other analysis techniques such as TEM (38)(39). By milling a thin lamella of a region of interest that can be attached to a micromanipulator by welding using the instrument's gas injection system (GIS). The lamella can then be lifted out from the material and placed on a suitable sample holder such as a half grid. The ion milling can then be used to make the specimen sufficiently thin for TEM analysis. This method allows for site specific specimen preparation where a region of interest can be selected with a high degree of control compared to previous techniques where a sufficiently thin region of a material was obtained by grinding the sample. However, note should be taken of the risk of the ion beam damaging or contaminating the specimen (40).

2.5. Atom probe tomography

APT is an analytical method that provides three dimensional chemical compositional information about a material with near atomic scale spatial resolution (41)(42). The technique is developed from the Field Ion Microscope, FIM, invented by E. W. Müller in the middle of the 20th century.

By utilizing the field evaporation phenomenon, where surface atoms can be individually removed by breaking the atomic bonds to surrounding atoms when an electric potential is applied to a needle-shaped sample with a sufficiently small apex radius, atoms are removed from the surface. The removed atoms become ionized during the field evaporation and travel along the electric potential and are collected by a position sensitive detector. By triggering the evaporation with either a laser or voltage pulse, the time of flight of the ions can be measured. After field evaporation, the ions can be further post-ionized to reach higher charge states, which has consequences for the analysis as the time of flight is related to the ion's mass-to-charge state ratio rather than its mass. The principle of the instrumentation used can be seen in Figure 1.
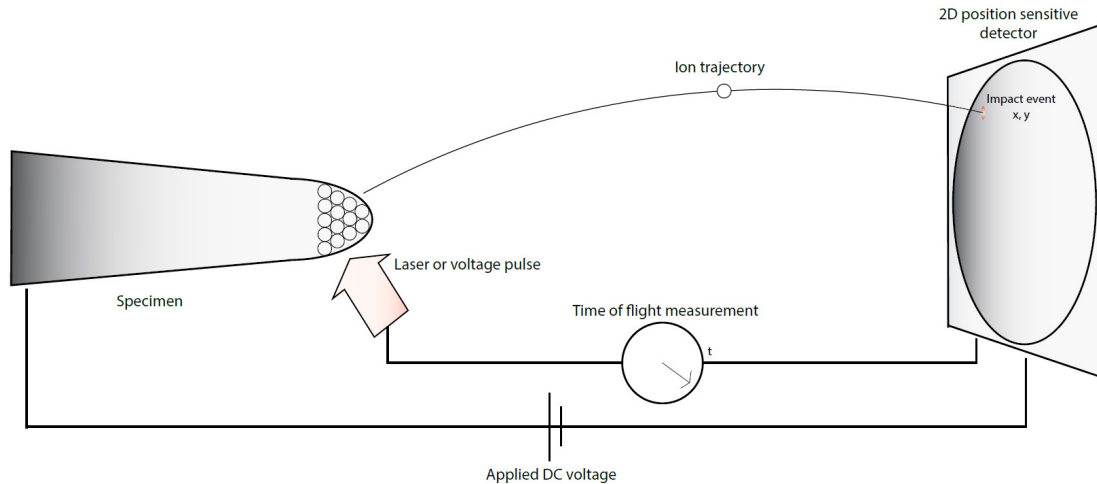
Figure 1: Schematic overview of the APT working principle. Individual atoms from a cryogenically cooled specimen are evaporated by a laser or voltage pulse and by post-ionization accelerated towards a position sensitive detector as their time of flight is measured.

For a surface atom to be field evaporated, the field applied to it needs to surpass the material specific evaporation field, a property that varies for different elements in different materials, often in the range of tens of V/nm. In order to identify the atoms collected they are characterized using time of flight mass spectrometry. To ensure that the correct time of flight is measured, the evaporation of atoms is controlled by pulsing, which can be either by increasing the potential at the pulse or illuminating the specimen with a laser. At the standing voltage (DC field), the potential is held below the field required for evaporation and by pulsing the potential, so the field experienced by the apex atoms is increased above the evaporation field, as illustrated by the graph in Figure 2, individual atoms can be evaporated. Field evaporation can also be thermally assisted, meaning that by a laser pulse, the temperature at the specimen apex is temporarily increased so the applied voltage is sufficient to field evaporate individual apex atoms.
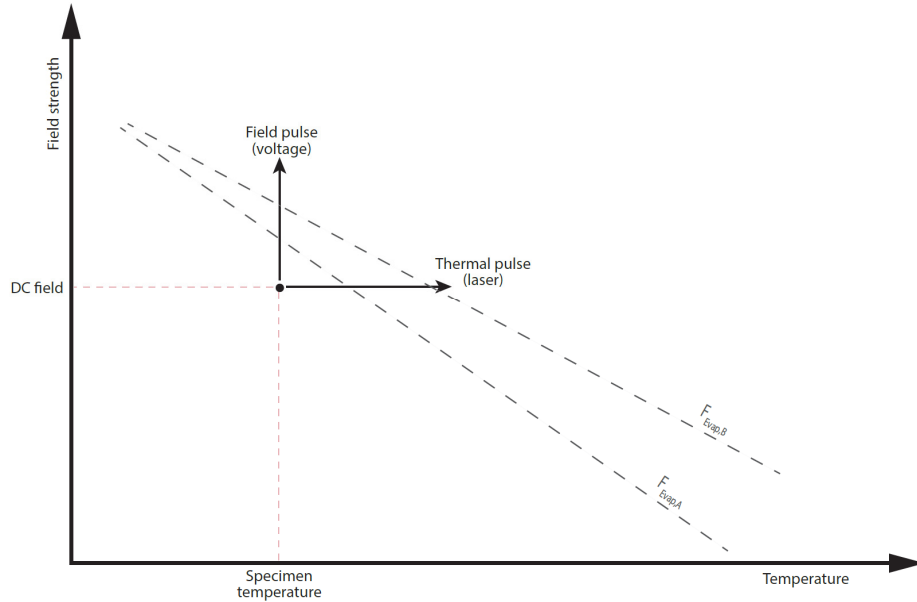
Figure 2: Schematic illustration of the temperature dependence on the evaporation field for two elements A and B.

In a specimen containing two or more elements with different evaporation fields, preferential evaporation of the element with the lower evaporation field can occur (43). This means that the DC field required to reach the desired evaporation rate from the specimen with the set pulse fraction is high enough to evaporate atoms of the element with lower evaporation field between the pulses. These atoms when evaporated and ionized will arrive at the detector with an incorrectly measured time of flight, and consequently end up in the background of the mass spectrum. This phenomenon is a main source of compositional bias in APT measurements but can be avoided by a proper selection of temperature and voltage pulse fraction or laser pulse energy.

2.5.1.Specimen preparation

The first made APT specimen were prepared by electropolishing, where a wire is etched to the required sharp needle shape by applying a current to it while it is dipped in a thin layer of an electrolyte solution (44). The wire is etched by moving it through the electrolyte layer and it will be made thinner until it ruptures, the radius at the breaking point will often be below 100 nm, low enough to be able to trigger field evaporation in an APT instrument.

The development of the dual beam focused-ion-beam scanning electron microscopes, FIB-SEMs, has made site specific sample preparation possible while also allowing APT specimen to be prepared from other materials than metals (45). This in combination with the laser assisted atom probe has led to a dramatic increase in research utilizing APT in the last decades. While electropolishing is limited to conductive metals, the main limitations for FIB-SEM sample preparation is that the material can stand the vacuum inside the SEM chamber. Non-conductive materials can be sputter coated with a few nm thick metal layer, which is routinely done for SEM analysis of such samples. The established sample preparation protocol consists of ion milling to separate a cantilever about 20 μm long and lifting it out using a micromanipulator that is attached using the FIB's gas injection system (GIS). Segments of the lift-out is placed on flat top posts on a micro-tip coupon also using the GIS and sharpened into a specimen with an apex radius below 50 nm using annular ion milling with gradually reduced inner diameters. The protocol is illustrated in Figure 3.
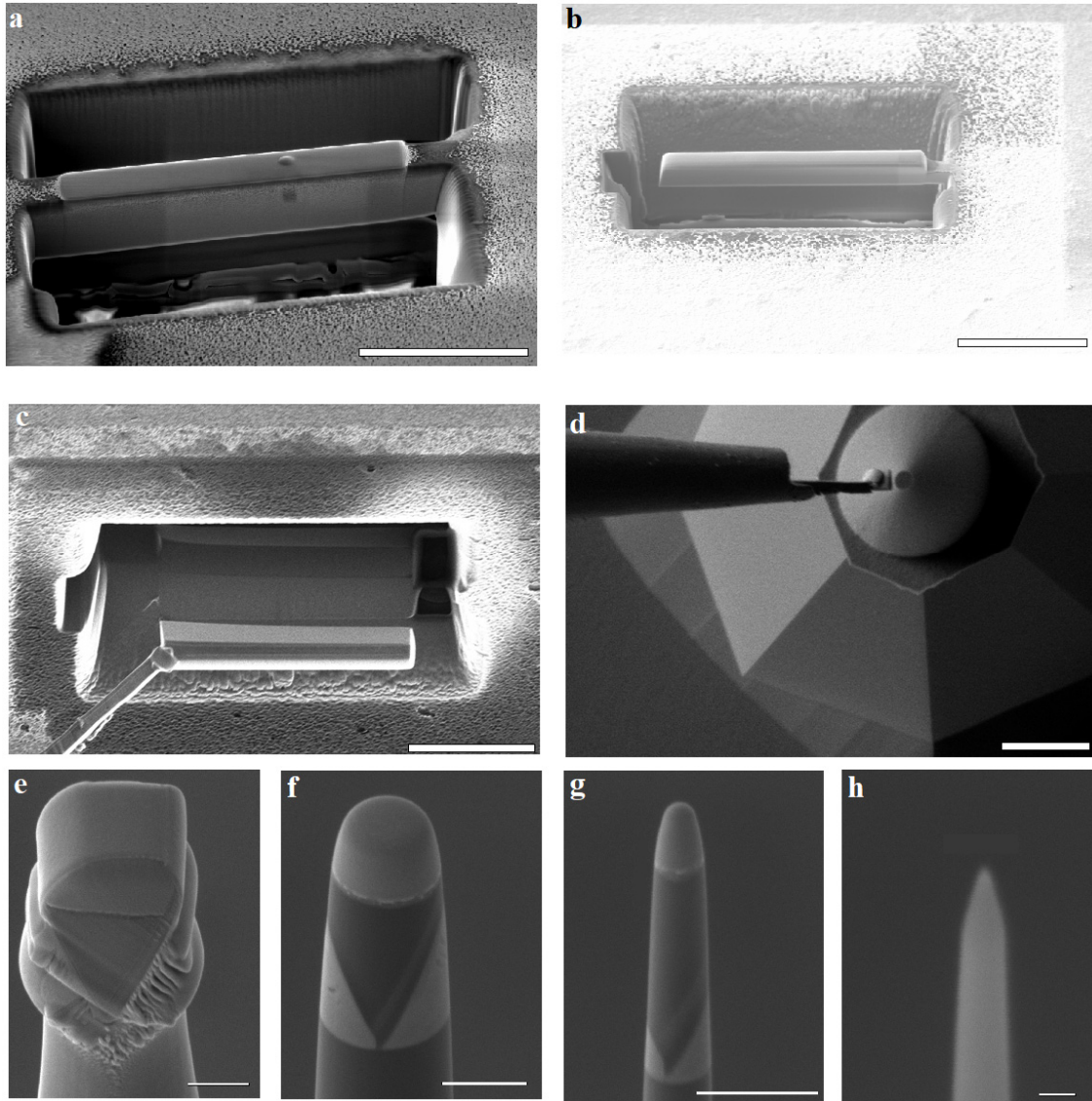
Figure 3: Procedure for the standardized FIB-SEM lift-out protocol for APT sample preparation. In image a-d the scale bar is 10 µm. In image e-g the scale bar is 1 µm. In image h the scale bar is 100 nm. a: A region is selected for lift-out and separated by ion milling of trenches at a 30° angle around a 2 x 20 µm area covered by a protective coating deposited by the instrument's gas injection system. b: One of the connections between the lift-out and remaining sample is milled away. c: A micromanipulator is inserted and attached by Pt-deposition. The lift-out is detached from the sample by milling away the remaining connection. d: The lift-out is placed in 2 µm segments by Pt-deposition to premanufactured silicon flat-top posts on a coupon (Cameca Scientific Instruments) and separated by ion milling. e: Lift-out segment on a silicon flat-top post. f: By annular milling with the specimen perpendicular to the ion beam, and gradually reduced inner diameter, a APT specimen is polished. g: Further polishing of the APT specimen until the protective Pt-layer is removed. h: The final polished APT specimen after a cleaning step by ion milling at a lower acceleration voltage.

2.5.2. APT analysis

In order to perform analysis by APT of the needle shaped specimen, the specimen first has to be introduced in the ultra-high vacuum analysis chamber, with pressures of 10^{-8} to 10^{-9} Pa, and cooled down to cryogenic temperatures, $20 - 80$ K. It is then aligned to the detector, or in the case of the local electrode atom probe, LEAP, systems, the local electrode, to ensure that the evaporated ions reach the detector with the correct trajectories and flight length. To start the analysis, a voltage is applied, and the laser or voltage pulsing starts. The voltage is increased until the desired detection rate, meaning the number of pulses that generates a detector event, is reached – often in the range of 0.2 to 2 %. The system is then set to automatically increase the voltage to maintain this detection rate as the specimen is evaporated and its radius increases along the shank. In the laser pulsing mode, the laser is scanned over the specimen to find the apex, as the location where the highest detection rate is achieved. The increased voltage causes most analyses to end with the fracture of the specimen, as the high field introduces a Maxwell stress on the specimen which increases as the specimen radius increases (2).

2.5.3. Data reconstruction

Each detection event is stored as a data point containing the x- and y-coordinates on the detector, the time of flight and the sequence. The time of flight gives the mass to charge ratio, M, of the ion by the equation (1),

$$M = \frac{m}{n} = 2eV\left(\frac{t_f}{L}\right)^2 \tag{1}$$

where m is the ion's mass, n its charge, e the elementary charge of the electron, V the applied voltage, L is the flight length and t_f the time of flight (41). During the reconstruction protocol, the data is arranged in a mass spectrum, where some

characteristic peaks can be identified and fitted to the correct ion mass, often given in Daltons.

A reconstruction algorithm is used to transfer the raw APT data to 3D spatial coordinates, real space data in the specimen. In order to get an as accurate reconstruction of the specimen as possible, information is needed of the specimen shape. The relationship between evaporation field and the applied voltage at the moment of evaporation can be used to obtain the specimen radius needed for the reconstruction, as seen in equation (2),

$$R_0 = \frac{V}{kF} \tag{2}$$

where F is the evaporation field of the material studied, R_0 is the initial tip radius and V is the applied voltage. The k-factor is dependent on geometrical considerations such as the specimen shank angle and radius (46). This allows the use of the voltage profile of the analysis to create the 3D reconstruction. Other methods use a known initial tip radius and specimen shank angle to form the reconstruction.

2.5.4.Applications of APT

APT was first used to study bulk compositions of metallic materials, due to the constraints imposed by the need for conductivity to voltage pulse and the limitations of the electropolishing method used for specimen preparation. The introduction of laser pulsing to thermally assist field evaporation, and later on the FIB method for site specific sample preparation led to APT being accessible to analyse more materials and to answer more questions. Today, the method is used to study also semiconductors, geological materials, biominerals and work is conducted to make methodology accessible to study soft materials (42).

3. Methodology

In the following chapter, the experimental procedures for the work conducted in this thesis work is presented. First the sample preparation is described, followed by the use of the various applied characterization techniques.

3.1. Nanoparticle synthesis

Gold nanoparticles were synthesised using a seed-growth procedure developed from the Trukevich method (47). 100 ml 1.0 mM $HAuCl_4$ solution was added to 100 ml milli-Q water and heated to 100 °C under stirring in order to prepare a gold seed solution. After the solution started boiling, 10 ml 38 mM sodium citrate was added, and the solution was kept at the boiling temperature for 80 min before being cooled down to room temperature. A growth solution was prepared by adding 2 ml 20 mM $HAuCl_4$ to 85 ml milli-Q water under stirring, followed by addition of 200 µl 10 mM $AgNO_3$. All silver nitrate containing solutions were wrapped in foil to protect them from light. Growth of gold nanoparticles to the desired size was done by adding 7.5 ml of the previously prepared seed solution to the growth solution. Nanoparticle growth was controlled by 15 ml 5.3 mM ascorbic acid at a rate of 0.6 ml/min. The final solution was left stirring after completed synthesis.

3.2. Nanoparticle surface modification

Substrates were modified with the prepared nanoparticles to form a platform designed for subsequent protein binding and silica embedding (more information about this below). Several commonly used linker compounds were assessed for their ability to provide a high surface coverage of the previously prepared gold nanoparticles, with a low nearest neighbour distance but without any aggregation of particles.

The surfaces used were silicon wafers, coated with a 10 nm thick chromium film, acquired from Substrata, Ångström Engineering. In most cases, the wafers were heat treated at 600 °C prior to any work in order to ensure good adhesion between the chromium layer and the underlaying silicon, as well as the silica in the final samples. The wafers were cleaned by isopropanol followed by ethanol in an ultrasonic bath for 30 min each, and then treated in a UV/O$_3$-oven to make the surface ready for modification. The self-assembled monolayers could then be placed on the surfaces by placing the wafers in a 2 % (3-aminopropyl)-triethoxysilane (APTES), (3-mecaptopropyl)-trimethoxysilane (MPTMS) or propylamine in toluene solution. After 45 min the surfaces were transferred to ethanol and then milli-Q water before being placed in a nanoparticle solution for 1 h. After this incubation, the wafers were transferred to milli-Q water, followed by ethanol and toluene, and dried from the toluene to remove the risk of the nanoparticles moving on the surface during drying.

3.3. Protein binding and silica embedding

The nanoparticle modified surfaces were cleaned in a plasma cleaner to remove any remaining organic material from the surface modification process or other contamination. The surfaces were subsequently covered by 25 µl protein solution for 3 h, consisting of thiol modified streptavidin acquired from Nanocs in PBS buffer prepared from pellets by SigmaAldrich dissolved in milli-Q water. After this, any proteins not attached to the surfaces were removed by gently washing the surfaces with PBS buffer. Following this, the surfaces were incubated in a biotin modified gold nanoparticle solution obtained from Nanopartz for another 3 h. Both incubation steps were carried out in a saturated atmosphere by placing the substrates under a lid next to an open water container, in order to avoid evaporation of the small volumes of liquid. A schematic of the final material with the different components that are added stepwise is presented in Figure 4.
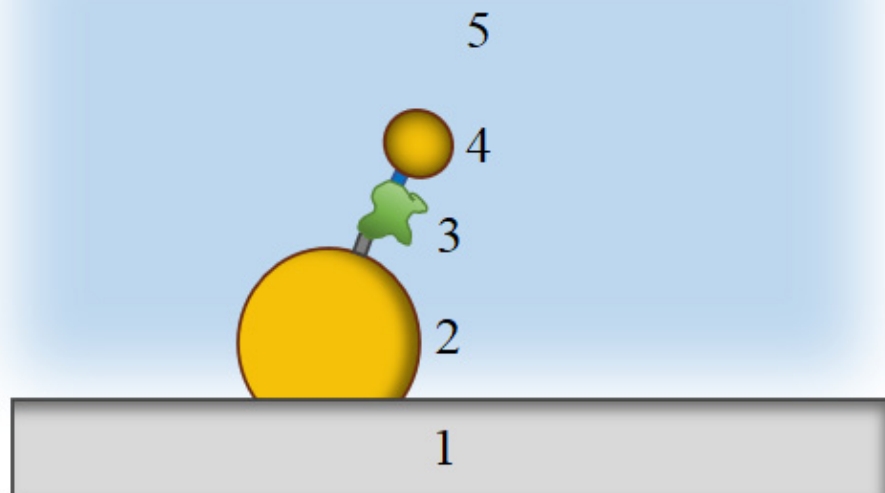
Figure 4: Schematic overview of the prepared materials. 1: Silicon wafer with 10 nm Cr-film. 2: Gold nanoparticle. 3: Thiol modified streptavidin. 4: Biotin modified gold nanoparticle. 5: Silica film.

The protein modified surfaces could then be stored in buffer until silica embedding. A silica gel was prepared by running an aqueous water glass solution using sodium silicate, Sigma-Aldrich, diluted in milli-Q in a 1:3 ratio, through an ion-exchange column to adjust the pH from basic to neutral. The column was prepared in a Luger 5 ml syringe, by placing 0.25 g glass wool in the bottom, under a membrane from an identical syringe with a 2 mm hole cut through it. On top of this, 1.5 g ion exchange beads (Dowex 50WX8 hydrogen form 50-100 mesh) were placed and stored in NaOH [4M]. Prior to use of the ion exchange column, the NaOH used for storage was rinsed with milli-Q water and the ion exchange beads were activated with 4 ml HCl [1M]. The column was then calibrated by rinsing of milli-Q in 3 ml increments until the extrude had a pH around 5. Then 1.5 ml of the water glass could be run through the column to obtain a pH at an acceptable neutral level. The pH adjusted water glass solution was then coated on the modified substrates by spin coating a volume of 75 μl at 1750 rpm for 90 sec. The substrates were finally dried at 37 °C to obtain the silica embedding presented in Figure 4.

3.4. Hydroxyapatite nanoparticle embedding

Samples with hydroxyapatite nanoparticles (nanoHA) on a titanium substrate were provided by Promimic AB. An aqueous dispersion containing calcium phosphate nanoparticles were spun on titanium surfaces followed by a heat treatment. These surfaces were then sputter coated with chromium using a Leica EM ACE600, depositing a 150 nm thick film embedding the particles under a sputter vacuum of $8 \cdot 10^{-3}$ mbar at 110 mA.

3.5. SEM imaging

The samples that were surface modified by nanoparticles were characterized using SEM imaging. The instrument used was an LEO Ultra 55 operating with acceleration voltages from 5 to 20 kV. The detectors used was an in-lens secondary electron detector, requiring a working distance of 5 mm and providing high resolution surface topographic information.

3.6. TEM and APT sample preparation

Specimens for both TEM and APT analysis were prepared using standardized lift-out techniques (39)(38) (45)(48). Prior to the lift-out procedure, the samples were covered with a protective layer deposited by sputter coating gold or chromium, in order to protect the region of interests from damage caused by the gallium ion milling (49). Using a FIB model FEI Versa3D LoVac DualBeam, a site of interest is identified and selected for lift-out. The lift-outs were generally made around the middle of the previously prepared samples, where the silica film appeared to be the smoothest. The sites of interest were first covered with a protective platinum film, deposited by the FIB's GIS from a precursor gas (methyl-cyclopentadienyl) trimethyl platinum. The strip was deposited using the electron beam at 5 kV first and then the Ga^+ ion beam at 30 kV, 50 pA followed by 500 pA until a 1 -1.5 μm Pt film covered the region to be lifted out. The lift-out size was 1.5 x 12 μm for the TEM specimens and 2 x 24 μm for the APT specimens.

Trenches were milled around the long edges of the Pt covered regions using the Ga^+ ion beam operating at 30 kV, 5 – 7 nA followed by a cleaning step at 1 nA. For the APT lift-out, the stage was placed at an angle of 30° with regards to the ion beam during milling of trenches, to form a more wedge-shaped lift-out while the TEM sample was milled with the stage perpendicular to the ion beam, forming a lamella.

Following this, a cut is made using the ion beam at 1 – 3 nA freeing the wedge-shaped APT lift-out on one side. For the TEM samples, a so-called U-cut is made, leaving the lamella stuck to the rest of the sample on only one side in a similar fashion. At this point, the Omniprobe micromanipulator is inserted and welded to the specimen using Pt deposition. Finally, the lift-out can be cut loose from the sample and removed by retracting the micromanipulator.

The triangular wedge-shaped APT lift out was placed on a silicon flat top coupon from Cameca Instruments by using the Pt-deposition system to weld a roughly 2 μm long section to a flat top post and cutting it loose using the ion-beam. This way, a normal 24 μm lift-out can be used for at least six APT specimens. The lift-outs are polished to needle shaped specimens after fixation to the flat top posts using annular milling by the ion beam with gradually reduced inner radius and currents while the stage is at 52°, meaning that the coupon is perpendicular to the ion beam. The first milling is done at 30 kV, 1 nA with an outer radius of 6 μm and inner radius at 3 μm until the specimen is at least 10 μm tall to prevent field evaporation from secondary tips during the APT analysis. The last milling step at 30 kV is carried out with an inner diameter of 0.15 μm at 50 pA. Following this, the milling is continued at 5 kV and 48 pA without an inner diameter until the protective Pt-layer is removed. Then the specimen is made as sharp as possible at lower currents, 16 pA - 2 pA, before polishing at 2 kV for a few sec to remove Ga^+-ions that have been implanted in the specimen during milling.

The TEM-lift out is welded to a cupper half grid from TED Pella by Pt-deposition. It is then milled using a cleaning cross section pattern, first at 30 kV and 1 nA but in subsequential steps with lower currents down to 50 pA. This is done until the protective Pt-layer is removed, and the sample is sufficiently thin to be transparent for electrons at the energies used in TEM at the region of interest.

3.7. TEM imaging

The TEM lift-outs were studied using a FEI Tecnai T20 operating at 200 kV and a FEI Titan 80-300 operating at 300 kV. For brightfield imaging the instruments were operated in TEM-mode. In order to do chemical characterisation by energy-dispersive X-ray spectroscopy (EDX), imaging was done in HAADF-STEM mode using the FEI Titan 80-300.

3.8. APT analysis

The APT specimens from samples with silica embedded gold and proteins were analysed using a LEAP 3000X HR from Imago Scientific Instruments, equipped with a green laser operating at a wavelength of 532 nm. The experimental parameters used were 55 K, laser energies at 0.2 – 0.3 nJ with the pulse frequency 100 kHz and evaporation rate set to 0.2 %. The collected data was reconstructed by IVAS 3.6.8 from Cameca using voltage profile.

The specimens from nanoHA modified titanium surfaces were analysed using a LEAP 5000 XS from Cameca Scientific Instruments operated in laser mode using a wavelength of 355 nm. The experimental parameters used were 60 K, laser energies at 65 pJ or 95 pJ giving an effective pulse fraction of approximately 25 % (50), and a detection rate set at 1 to 2 %. The data was reconstructed using Cameca IVAS 3.6.12 based on the tip profile of the specimen and analysed using Cameca IVAS 3.6.8.

4. Results and discussion

In the following chapter, the results from the experimental work conducted will be presented and discussed. The nanoparticle synthesis is presented first, followed by the material assembly, and finally the TEM and APT analysis.

4.1. Nanoparticle and protein attachment to surfaces

Several methods of attaching nanoparticles to substrate surfaces prior to embedding and analysis were evaluated in this work. By assessing the surface coverage of particles with regard to the amount of surface covered, average distance between the particles and as low amount of aggregation as possible, the success of the attachment was determined. When comparing the surfaces modified with a self-assembled monolayer of either APTES (Figure 5 a), MPTMS (Figure 5 b) or propylamine (Figure 5 c), it was found that the surface modified with MPTMS gave the highest surface coverage, meaning the highest number of nanoparticles in a given area of the surface.
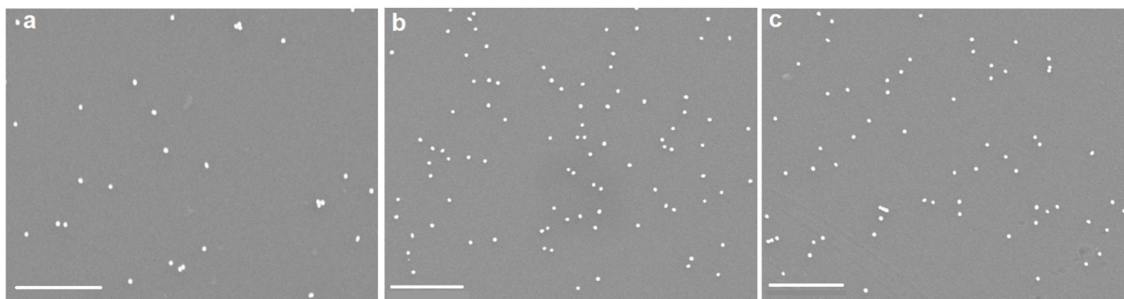
Figure 5: Surface modification with gold nanoparticles using self-assembled monolayer of different linker molecules. a: Surface with APTES self-assembled monolayer. b: Surface with MPTMS self-assembled monolayer. c: Surface with propylamine self-assembled monolayer. Scale bars: 1 μm.

By further developing the protocol, a satisfactory surface coverage was achieved when attaching the nanoparticles to an MPTMS modified surface that had been heat treated prior to modification and where the nanoparticle incubation was carried out for a sufficient time. The resulting coverage can be seen in Figure 6, where information regarding the particle size distribution (Figure 7 a) and nearest

neighbour distances (Figure 7 b) was extracted through image analysis. The particle size distribution was found to be narrow with an average diameter of 32 nm and the average nearest neighbour distance was 58 nm, which sufficiently short to likely find at least one nanoparticle in an APT specimen.
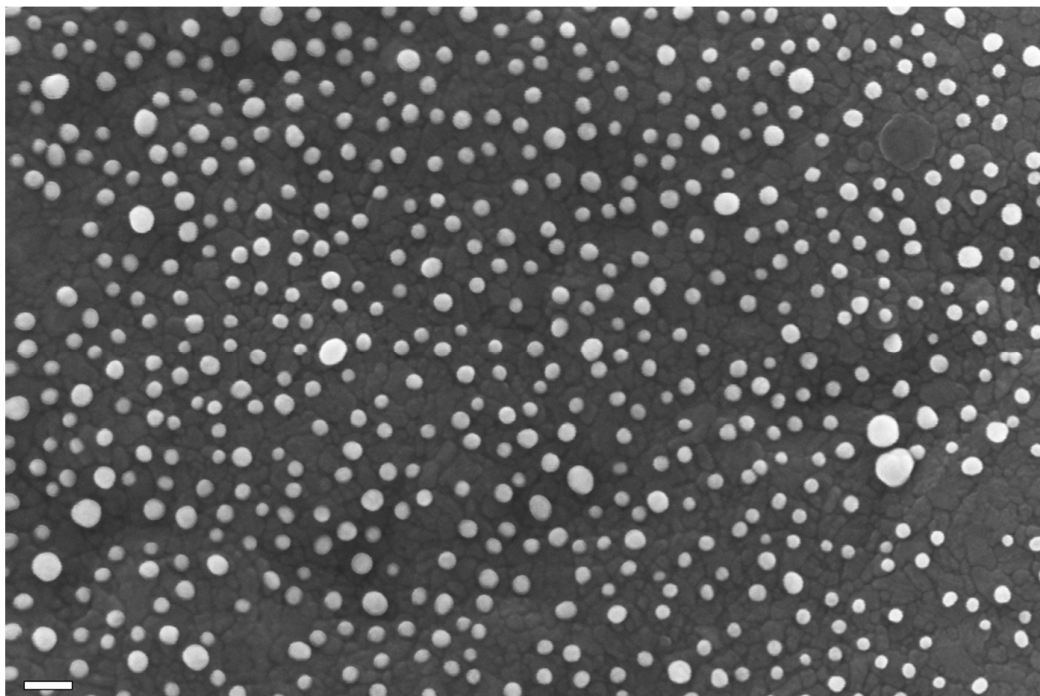

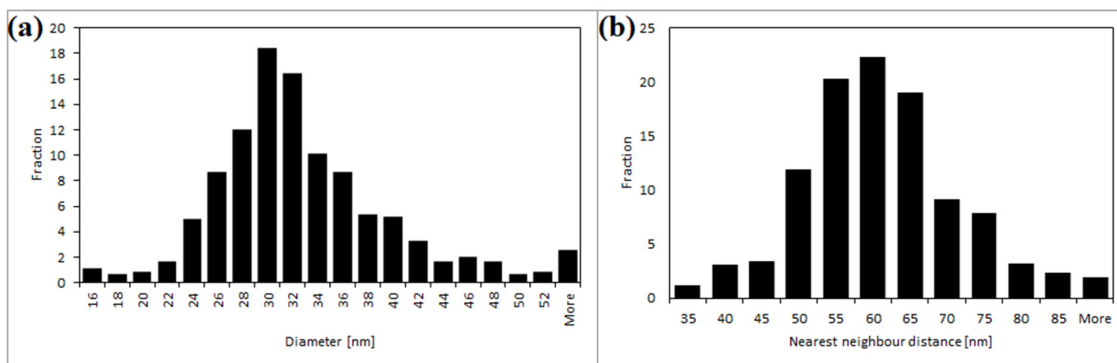*Figure 6: SEM micrograph of gold nanoparticle silicon wafer substrate. Scale bar: 100 nm.*

Figure 7: a: Distribution of nanoparticle diameters. b: Distribution of nearest neighbour distances of nanoparticles.

Similar surface coverage results were also achieved by base piranha cleaning of a surface instead of modifying it with MPTMS, indicating that nanoparticle immobilization by electrostatic interactions could also be a possible method. However, since the covalent binding from chemisorption generally is stronger than the electrostatic interactions, it was preferred considering the similar surface

coverage and the risk of removing the particles when later spin coating with water glass solution.

After obtaining a surface with a satisfactory nanoparticle coverage, it was attempted to attach the thiol modified streptavidin protein to the particles and utilizing the affinity of the accessible thiol to the surface bound gold nanoparticles. The streptavidin binding was studied using biotin modified gold nanoparticles with a diameter of 10 nm which has an affinity to the streptavidin due to the strength of the streptavidin-biotin bond. In Figure 8, the material can be observed after modification with smaller biotin modified gold nanoparticles.
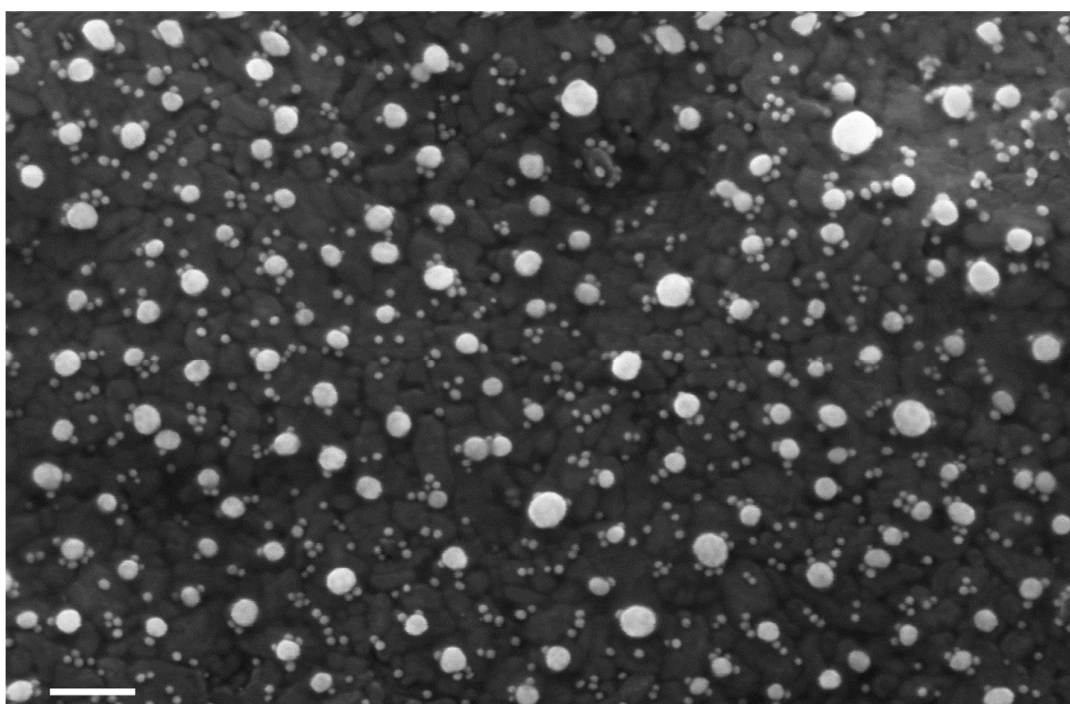
Figure 8: SEM micrograph of gold nanoparticle modified surface. After nanoparticle modification, thiol modified streptavidin. Scale bar: 100 nm.

When studying Figure 8, smaller nanoparticles can be seen surrounding the larger ones, possible indicative of successful thiol-streptavidin binding to the larger particles and consequently binding of biotin modified smaller particles. However, the smaller particles can also be observed to a significant degree covering the substrate surface. This suggests that preference for either the thiol-binding on the streptavidin or the biotin modified nanoparticles to the surface bound gold nanoparticle is not as strong as would be required to get binding to them exclusively.

4.2. Silica embedding of nanoparticle and protein modified surfaces

The surfaces modified with gold nanoparticles presented in the previous section were embedded in silica using the protocol of spin-coating pH-adjusted sodium silicate solution. The materials were then analysed using TEM on samples prepared by the lift-out protocol. TEM analysis of a cross section that has been lifted out gives more reliable information on the layers in the multi-layered structure of the materials, as can be seen in Figure 9 a. The silica layer appears bright, meaning low amount of electron scattering, consistent with what would be expected from a material containing the low atomic number elements silicon and oxygen. Comparatively, the chromium film, protective sputter coated gold layer and ion deposited platinum layer as well as the gold nanoparticles, all appear darker than the silica and silicon. The effect of heat treatment on the chromium layer is found as a distinct chromia layer on top of the chromium, illustrated in Figure 9 b.
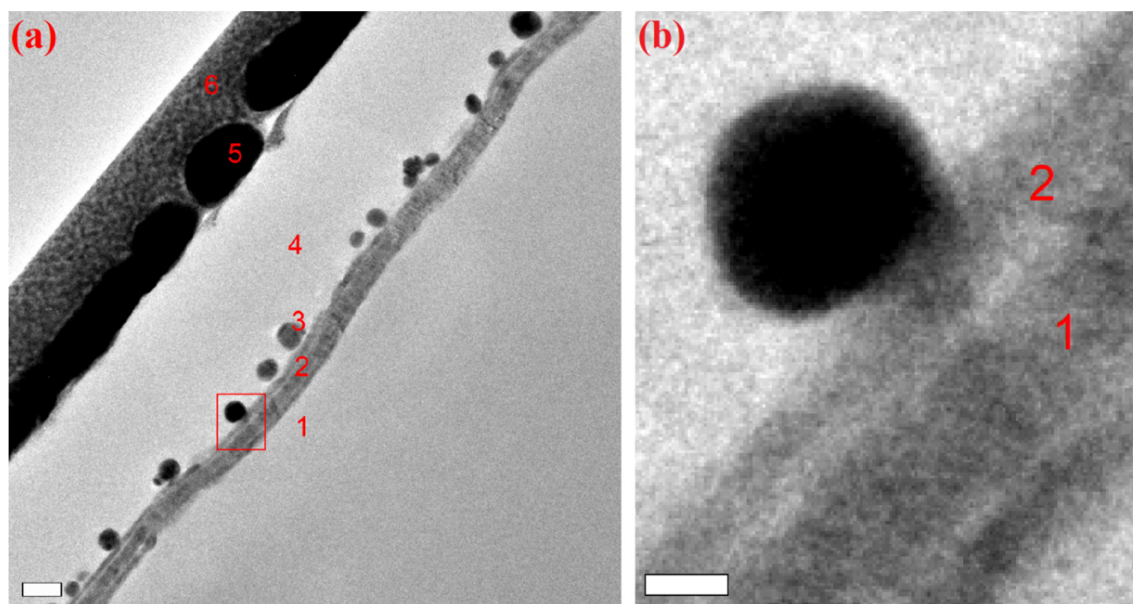
Figure 9: a: TEM micrograph showing an overview of gold nanoparticles embedded in a silica film. Labeled regions are 1: Silicon substrate, 2: Chromium layer, 3: Gold nanoparticle, 4: Spin-coated silica film, 5: Sputter coated protective gold layer, 6: GIS-deposited protective platinum-layer. Scale bar: 50 nm. b: Shows the region indicated by a box in (a) magnified. 1: Shows the chromium layer, 2: Shows the chromium oxide layer. Scale bar: 10 nm.

In the samples where the streptavidin protein and biotin tagged nanoparticles were attempted to be attached to the surface bound nanoparticles, varying results could be observed. Figure 10 shows how some of the surface bound nanoparticles have smaller nanoparticles adjacent to them. The smaller nanoparticles are in the size range expected for the biotin modified Au-NPs and the distance between the two particles is in the 5 nm range, similar to the reported size for streptavidin (51). It should, however, be noted that not all surface nanoparticles seem to have biotin-tagged nanoparticles bound to them and that some biotin-tagged nanoparticles are found on the substrate surface.
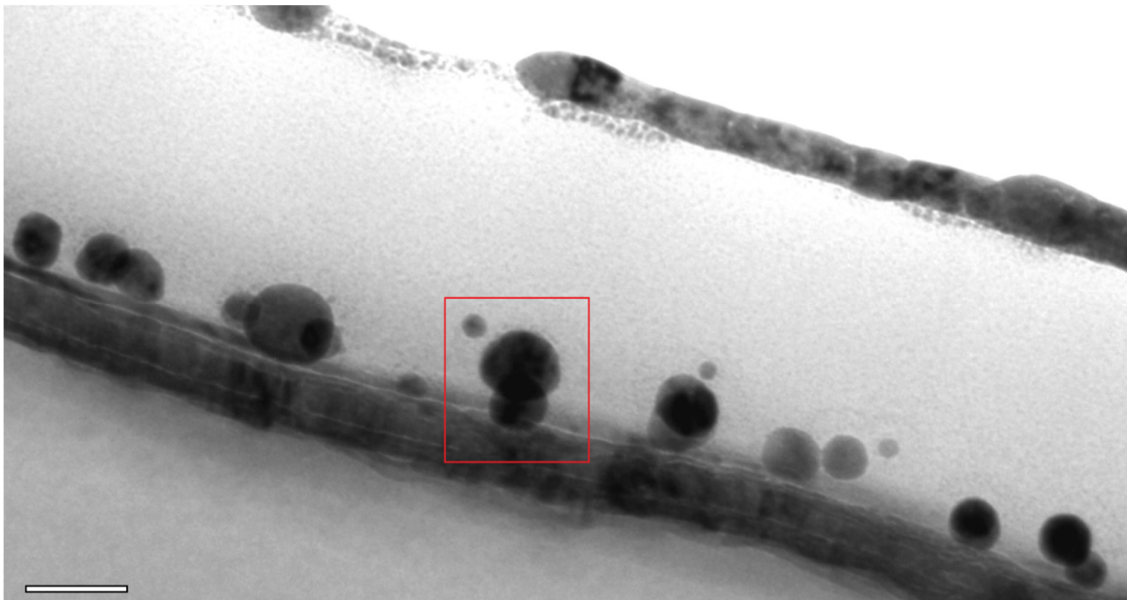
Figure 10: TEM micrograph of sample lifted-out from silica embedded surface with gold nanoparticles modified by thiol-streptavidin and biotinylated 10 nm gold nanoparticles. In the highlighted region, the distance between the larger and the smaller nanoparticle corresponds well to the size of the streptavidin-biotin complex. Scale bar: 50 nm.

4.3. Atom probe tomography on silica embedded nanoparticle and protein surfaces

From the same samples studied by TEM, APT specimens were prepared using the standardized lift-out protocol. Examples of such specimen can be seen in Figure 11. Using backscattered electrons to image the specimen, the gold caping layer as well as gold nanoparticles on the chromium film can be observed.
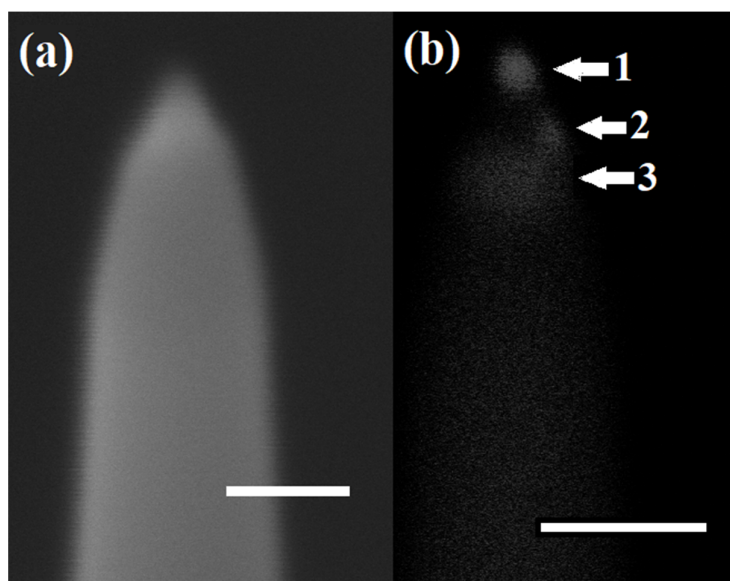

Figure 11: APT specimen prepared using FIB-SEM protocol imaged after polishing. a: A specimen imaged using secondary electrons. b: The same specimen imaged with backscattered electrons, high Z regions such as gold appear brighter. Regions indicated with arrows are 1: Protective gold-layer, 2: Gold nanoparticle, 3: Chromium layer. Scale bars: 100 nm.

In none of the analysed and reconstructed APT specimen, a biotin-streptavidin linked smaller nanoparticle was observed on the larger nanoparticles. This can to some extent be explained by the fact that these complexes were not formed on all particles, as seen in the TEM and SEM micrographs. Furthermore, it can be explained by that the silica embedding possibly was ripped off the specimen during analysis. This possible explanation is strengthened by the observation that very little silica was detected surrounding the gold nanoparticles during atom probe analysis, and that the specimen appeared to completely or partly fracture when the analysis entered the silica layer from the protective gold or chromium layer. A partial fracture is an event where a burst of ions from the sample is observed as a sudden increase in the detection rate, together with a rapid change

in the applied voltage, followed by new types of ions being detected and a new laser scan often being required to keep analysing the specimen. These events suggest that a layer of the specimen has been ripped off, while the underlaying layer still in intact and the specimen still is sharp enough to maintain field evaporation with a satisfactory detection rate at a reasonable applied voltage. Delamination of weak interfaces due to the high fields applied during APT is a common occurrence.

Regardless of the delamination of silica or not, several of the analysed specimens gave sufficient gold nanoparticle data. The reconstruction of one such analysis can be seen in Figure 12.
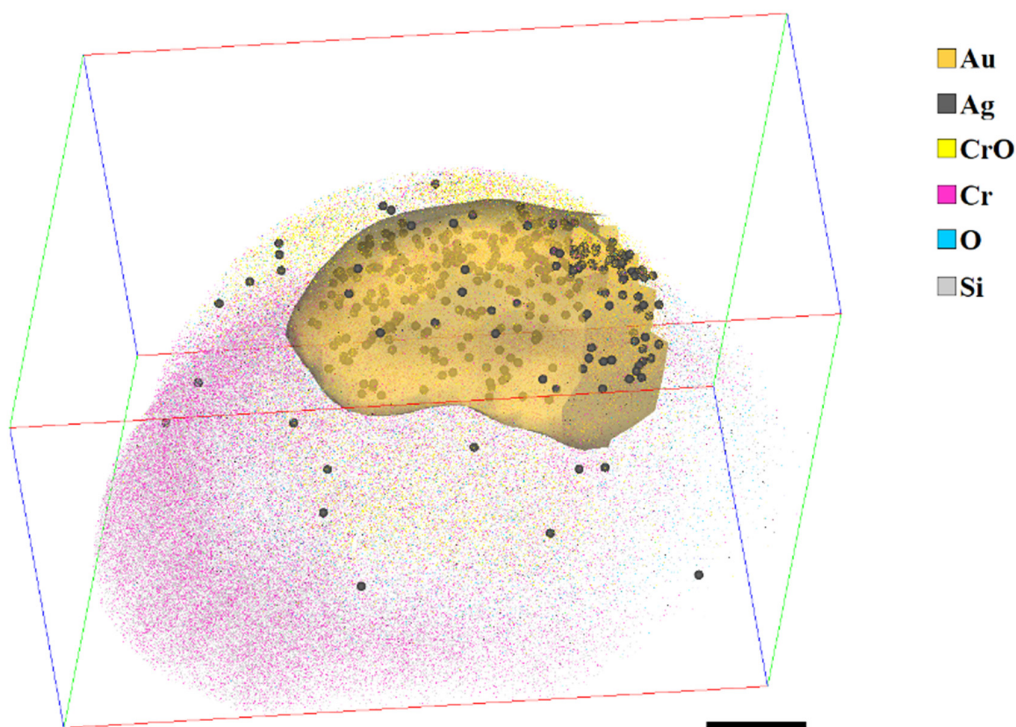
Figure 12: Reconstructed APT specimen showing a gold nanoparticle with an isosurface set at 25 % gold and silver highlighted as grey spheres. The surrounding chromia is seen in yellow and chromium in pink. Scale bar: 5 nm.

In some of the reconstructions, the shape of the nanoparticles appears to be elongated along the direction of analysis (Figure 13 a). This is a common artifact occurring when a region is surrounded by another with a higher evaporation field (52), as the gold nanoparticles with silica and chromia. By adjusting the

reconstruction   factor   *k*,   a   less   accentuated   elongated   could   be
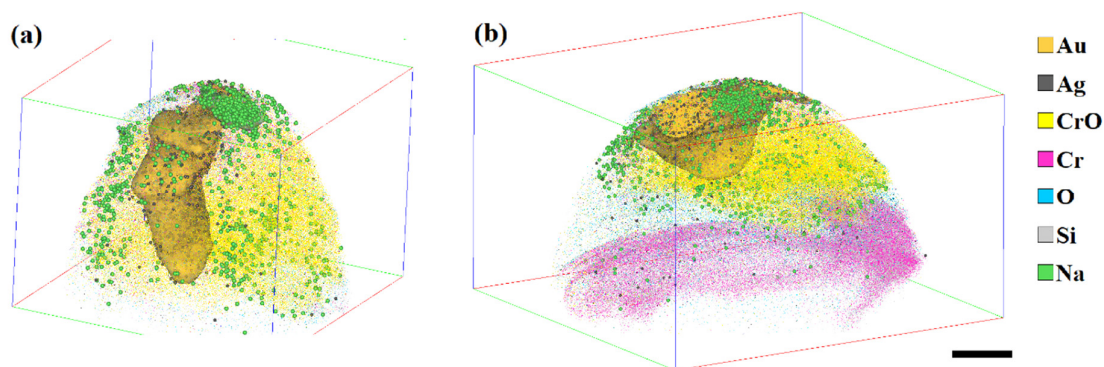achieved (Figure 13 b).

Figure 13: Reconstructions of analysed APT specimens containing gold nanoparticles made with different reconstruction factors. The gold isosurface is set at 25 %. Silver highlighted as grey spheres and sodium highlighted as green spheres. a: Reconstruction factor k set at 3.3. b: Reconstruction factor k set at 3.0. Scale bar: 10 nm.

In the reconstructed APT data, the gold nanoparticles appear to be embedded in chromia which is in disagreement with the material as it appears in the previously presented TEM micrographs. This can be explained by the proposed delamination of silica, as this would leave exposed gold nanoparticles on top of the chromia. Surrounding the nanoparticle, chromia would also be exposed and at the edges, high local fields can cause field evaporation of the surface atoms while the gold nanoparticle remains, causing the structure observed in the reconstructions. The chromia is detected as various molecular species such as mainly CrO^{2+} and CrO_2^{2+} but also Cr^{2+}, O^{1+}, O_2^{1+}, CrO_2^{1+}, and CrO_3^{1+}, which is in line with previously reported findings (53).

In some of the reconstructed specimens, sodium can be observed in clusters surrounding the gold nanoparticles, as seen in Figure 13. Sodium is present in several steps of the sample preparation process. Sodium citrate is used during the seed particle synthesis, it is in the buffer that the proteins are kept in, and traces can be present in the water glass solution after pH adjustment. The origin of the observed sodium cannot be said for certain but its presence in the specimen suggests that the method can be used to study ligands on nanoparticles, and as sodium citrate is used as a stabilizing ligand in solution, perhaps even for ligands in their hydrated state.

The distribution of silver within the gold nanoparticle was studied by making a rectangular volume intersecting the gold nanoparticle in the reconstruction (Figure 14 a). This volume was used to form a cross section in which the silver could be highlighted (Figure 14 b).
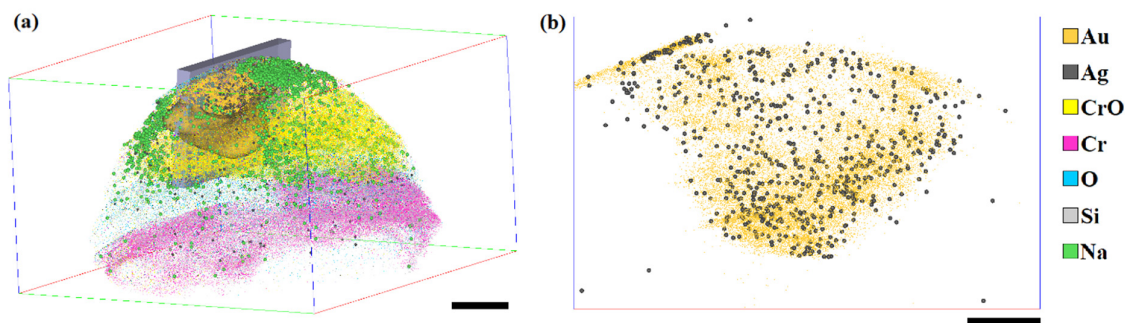

Figure 14: a: Introduction of a rectangular sub-volume to the reconstruction of the gold nanoparticle defined by the iso-surface in Figure 13 b. Scale bar: 10 nm. b: Cross-section of the gold nanoparticle defined by the sub-volume. The silver content in the particle is clearly visualized. The amount of silver in the region defined by the cross section is 2.3 % of the gold. Scale bar: 5 nm.

The silver distribution appears to be uneven with a preference to one facet of the nanoparticle. However, the gold content appears to be higher in the same region as well so this can also be explained by the evaporation behaviour of the specimen or microfractures occurring during analysis. The measured silver content in the specimens analysed varies between 2 – 4 %, which is below the 5 % molar ratio silver to gold in the seed growth solution. This suggests that not all silver in the seed growth solution ends up in the final nanoparticles. It is possible that some present silver is not be detected due to preferential evaporation, as pure silver has a lower evaporation field than pure gold (54). However, that does not necessarily mean that the silver has a lower evaporation field when in a gold nanoparticle.

4.4. Hydroxyapatite nanoparticles on titanium surfaces

The samples with nanoHA on titanium implant material were imaged with SEM prior to being embedded in sputter coated chromium and then analysed by TEM and APT. The SEM micrographs are seen in Figure 15.
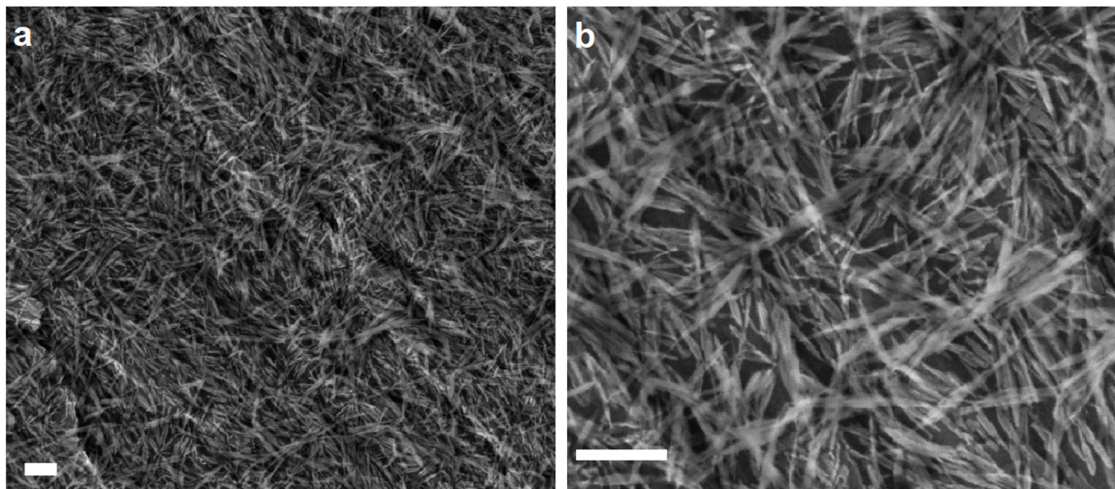

Figure 15: SEM micrographs of deposited nanoHA on titanium surfaces prior to chromium sputter coating. Scale bars: 200 nm.

In Figure 15 b, the rod-like structure of the deposited nanoHA can be seen, and they form a mesh-like pattern on the surface. The thickness of the nanoparticle layer is difficult to assess from the top view, but the titanium surface can be observed between the particles. Lift-outs prepared using FIB/SEM were analysed in TEM and the micrographs obtained by brightfield imaging can be seen in Figure 16 a. By a magnified view of the nanoHA region, the thickness of the nanoparticle layer could be assessed, and the titanium surface oxide was visible (Figure 16 b).
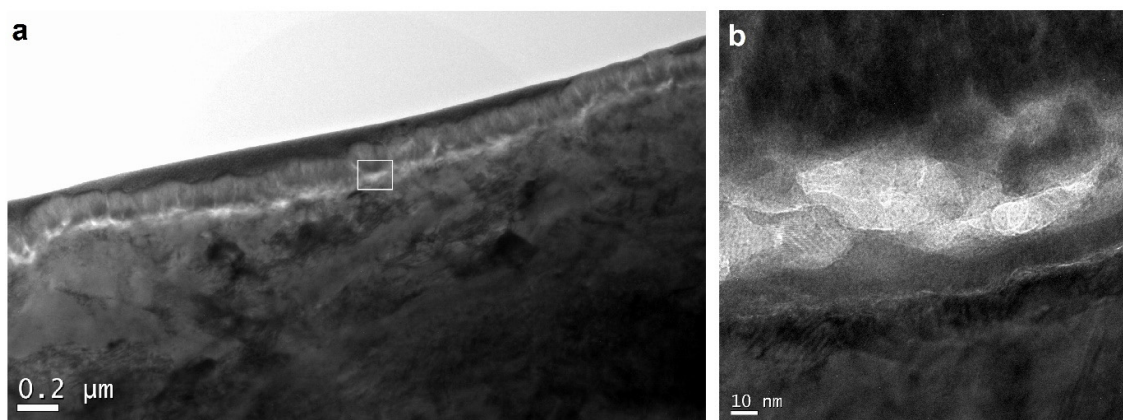
Figure 16: TEM micrograph of the nanoHA covered titanium. The sample surface is covered by a sputter coated chromium layer and a protective platinum layer deposited by the GIS during FIB/SEM sample preparation. a: Overview of the sample. The white box indicates the region magnified in b. b: NanoHA on the titanium surface. The surface oxide is visible beneath the nanoparticles.

The nanoHA appear as a bright region due to the lower electron scattering cross section of calcium and phosphorous compared to titanium and chromium. While individual nanoparticles are hard to discern due to their stacked structure and that many particles contribute to the 2D projection, the thickness of the nanoHA layer can be assessed to be around 20 nm. Underneath the nanoparticles, the titanium surface oxide is visible revealing a layer about 10 nm thick. By imaging in HAADF-STEM mode, the Z-contrast becomes more prominent (Figure 17 a), and in a magnified view of the nanoHA, regions were selected for EDX analysis (Figure 17 b).
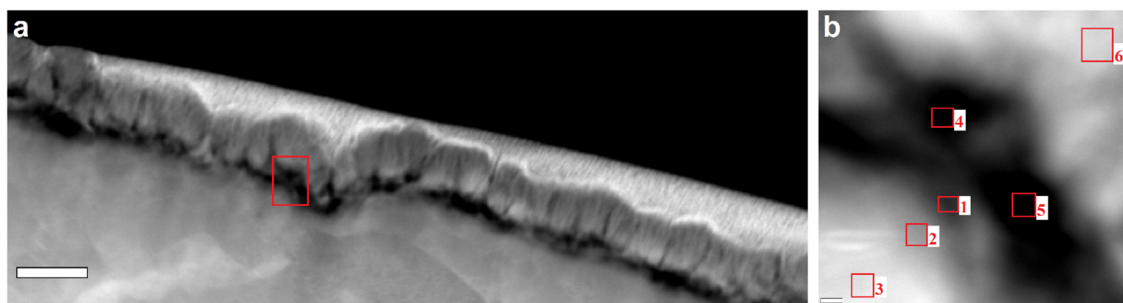

Figure 17: HAADF-STEM micrograph of the nanoHA covered titanium surface. a: Overview of the sample, at the bottom the titanium is seen, covered by nanoHA, sputter coated chromium and platinum from the FIB/SEM lift-out procedure. The red box highlights the region magnified in b. Scale bar: 200 nm. b: NanoHA region. The boxes 1-6 indicates the regions from which characteristic X-rays were collected for EDX analysis. Scale bar: 10 nm.

In darkfield imaging, the lower electron scattering of calcium and phosphorous makes the nanoHA region appear dark, while the other regions appear brighter. The calculated atomic % of the X-rays collected from the different regions in Figure 17 b are presented in Table 1.

Table 1: Atomic % quantified by the collected X-rays generated by HAADF-STEM from the areas highlighted in Figure 17 b: 1: Titanium oxide layer, 2: Just below titanium oxide, 3: Bulk titanium substrate, 4 and 5: Hydroxyapaite particles, 6: Protective chromium coating.

Area	Cr	Ti	O	Ca	P	C	Si	Cu
1	2	36	50	3	2	5	0.6	0.6
2	0.4	64	30	0.4	0.3	4	0.2	0.9
3	0.1	78	13	0.5	0.2	7	0.1	1
4	23	4	46	6	5	14	0.1	0.1
5	35	2	44	2	2	14	0.5	0.1
6	53	1	36	1	1	7	0.02	0.9

The EDX data (Table 1) shows that the nanoHA region appears to contain a significant amount of calcium and phosphorous. Based on the chemical composition of hydroxyapatite, roughly one third of the detected oxygen should originate from the hydroxyapatite. The remaining oxygen could originate from the oxidization of chromium. Depending on where in the nanoHA layer the X-rays are collected, different amounts of calcium and phosphorous are detected, as seen in the difference between area 4 and 5. In the titanium oxide, certain amounts of calcium and phosphorous are also detected, indicating that some atoms from these species have diffused into the surface oxide layer. Further down in the titanium, less to no calcium and phosphorous is detected. It should be noted that the spatial resolution of EDX is not completely reliable when observing areas in the size range studied here, as X-rays can be generated outside the region where the electron beam is focused. A high amount of carbon is detected in the nanoHA regions. Some carbon is expected due to the nanoHA as it can be carbonated when prepared in solution (55), however this does not explain the amounts detected. This can possibly be attributed to contaminations. The detected copper originates from the copper half-grid that the specimen was mounted to, and a silicon signal is generally expected from the detector itself.

The analysed APT specimens showed consistent results and a reconstruction of a specimen obtained with the laser energy set at 95 pJ are presented in Figure 18.

Analysis of the reconstructions proved challenging due to the high number of peaks in the mass spectrum; chromium and titanium have several isotopes and due to oxidization, they evaporate as various Cr_XO_Y and Ti_XO_Y species, respectively. The nanoHA also evaporates as several types of molecular species, consistent with previously reported results from analysis of bone and bone-like synthetic hydroxyapatite (56)(57).
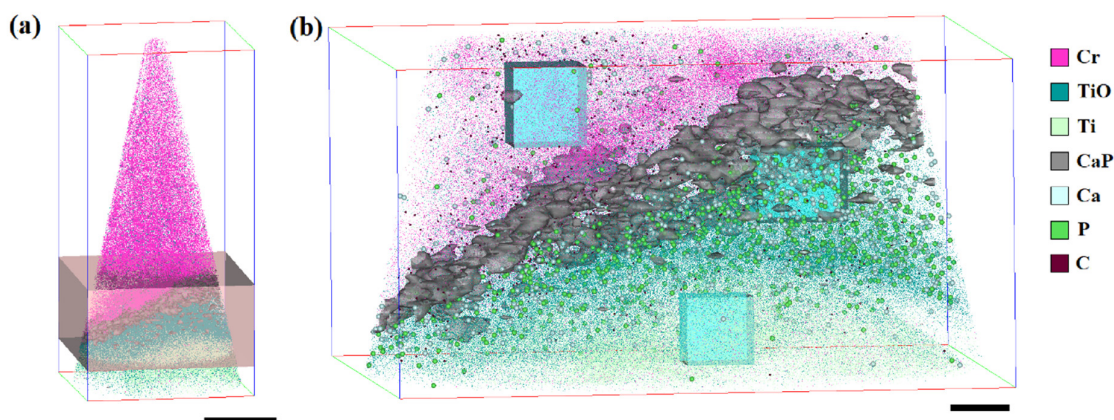

Figure 18: a: Reconstructed APT data from specimen analysed with the laser energy at 95 pJ. An isosurface set at 2 % CaP (71 Da) is in grey. Scale bar: 50 nm. b: Analysis of the region highlighted with a box in a. The three sub-boxes were used to analyse the composition of the chromium, titanium oxide, and titanium respectively. The species highlighted as Ca is the CaO_3^{2+} peak at 44 Da and the species highlighted as P is the $PO_3H_2^{2+}$ peak at 40.5 Da. Scale bar: 10 nm.

In the reconstructed data, a layer of ions at 71 Da was found at the chromium and titanium oxide interface, which were identified as CaP as no chromium or titanium originating ions are found at that mass-to-charge-state ratio. Surrounding the nanoparticle interface, mainly in the titanium oxide, ions at 44 Da and 40.5 Da occurred that were unambiguously identified as CaO_3^{2+} and $PO_3H_2^{2+}$, respectively. Carbon at 12 Da was also detected surrounding the interface, which is expected to originate from the nanoHA, which is partly carbonated. Using the boxes seen in Figure 18 b, composition analysis of the different regions could be made by studying the mass spectrum for the ions inside the defined regions and by that avoiding complications from having the chromium and titanium species in the same mass spectrum. The three mass spectra are presented in Figure 19 with major peaks highlighted. The bulk compositions from the analysed mass spectra are presented in Table 2.
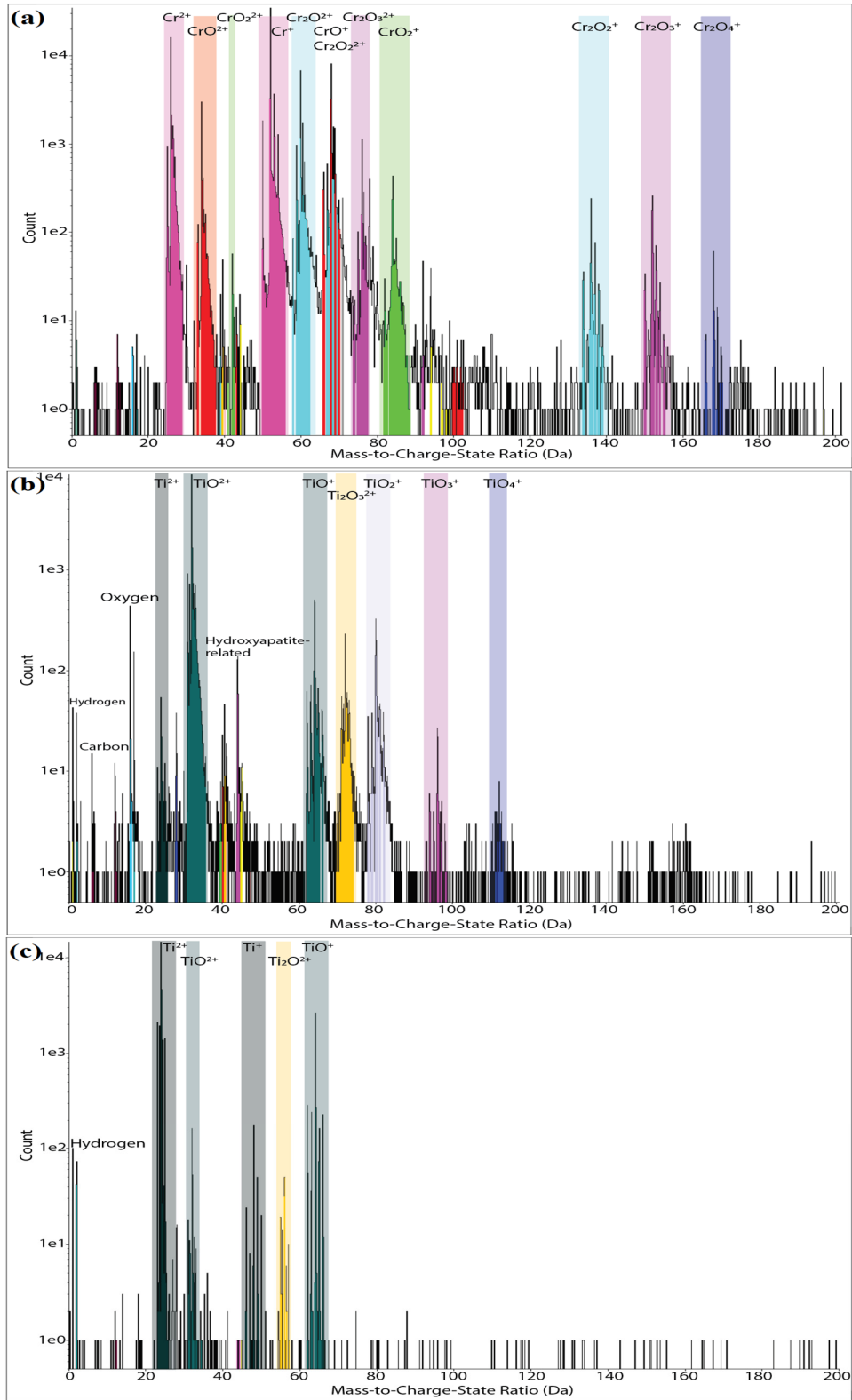
Figure 19: Mass spectra collected from the regions highlighted in Figure 18 b. Major peaks are highlighted. a: Mass spectrum from the chromium region. b: Mass spectrum from the titanium oxide. c: Mass spectrum from the titanium.

Table 2: Bulk composition (atomic %) of the different mass spectra presented in Figure 19, obtained by of the reconstructed APT data.

Region	Cr	Ti	O	Ca	P	C	H
Chromium	71.2	-	28.3	0.2	0.2	0.01	0.03
Titanium oxide	-	45.2	52.9	0.6	0.3	0.1	0.9
Titanium	-	85.9	12.5	0.01	0.01	0.01	1.6

The calcium and phosphorous ratio in the titanium oxide align somewhat with the expected stochiometric composition of hydroxyapatite, but the relative calcium is possibly slightly overestimated. The detected amounts are lower than the amounts measured by EDX, which can be explained by that a significant portion of the calcium and phosphorous also evaporate as species that overlap with titanium oxide or is lost due to preferential evaporation.

To study the presence of calcium and phosphorous throughout the interfaces and the titanium oxide layer, a cylinder was created in the reconstruction in Figure 18 b and used to make a one-dimensional concentration profile along the z-axis, presented in Figure 20. The placement of this cylinder and its chemical content is illustrated in Figure 21.

It can be seen that the carbon, calcium, and phosphorous content is the highest at the chromium and titanium oxide interface, where the nanoHA is located. The calcium and phosphorous appear to be quite constant throughout the oxide layer while none are present in the underlying titanium. This shows how the integration of atoms from the hydroxyapatite material into the titanium surface occurs during the material synthesis in a fashion that bears some resemblance to how bone grows into a titanium implant (58)(59). However, in the clinical example, there is a calcium enriched region at the top of the titanium surface oxide, which does not seem to be present in the analysed samples here. The lower-than-expected amount of calcium and phosphorous could also be attributed to preferential evaporation of these elements when the main elements of the specimen are chromium and titanium. When a lower laser power was used, meaning that the DC voltages needs to be higher to reach the same evaporation rate, an even lower

amount of calcium and phosphorous was detected, suggesting that at higher DC fields, more of these elements evaporate between the pulses and consequently do not get detected with the correct time of flight. This illustrates challenges with analysing these types of materials with APT and getting a correct measurement of the composition. However, APT data confirms the presence of calcium and phosphorous throughout the titanium surface oxide in a more reliable way than the HAADF-STEM EDX data.
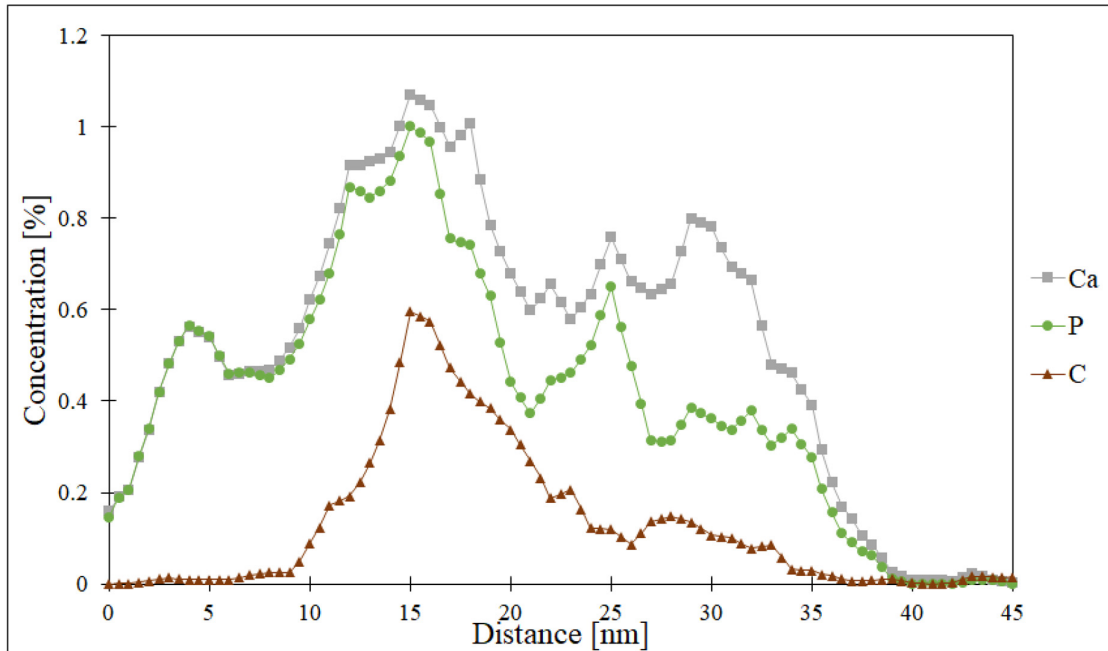

Figure 20: 1D concentration profile of the decomposed atomic Ca, P, and C content in the cylinder highlighted in Figure 21.

Legend:
- Cr (pink/magenta)
- TiO (teal)
- Ti (light green)
- CaP (grey)
- Ca (light blue)
- P (green)
- C (dark maroon)
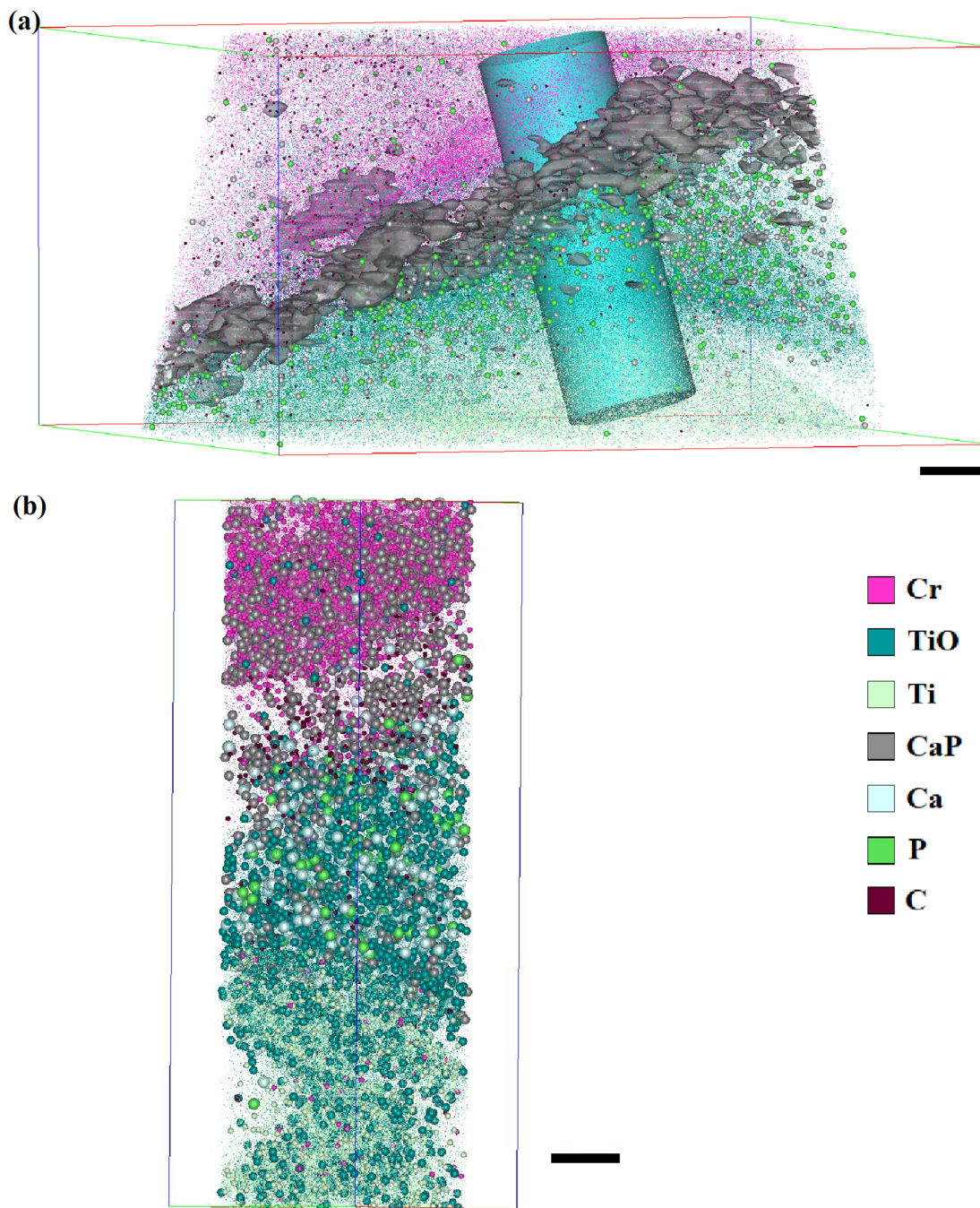
Figure 21: a: Region surrounding titanium surface oxide layer from the reconstructed APT analysis in Figure 19. Calcium and phosphate are highlighted, the grey isosurface highlights CaP (71 Da) at 2 %. The cylinder is used to measure the Ca and P content. Scale bar: 10 nm. b: Content of the cylinder highlighted in a. Scale bar: 5 nm. The species highlighted as Ca is the CaO_3^{2+} peak at 44 Da and the species highlighted as P is the $PO_3H_2^{2+}$ peak at 40.5 Da.

5. Conclusion and outlook

In this thesis, a sample preparation method to enable APT analysis of nanoparticles embedded in silica, which can allow for retention of ligands in the hydrated state has been developed. The method proved to allow for analysis of nanoparticles with a high likelihood of each APT specimen containing a particle thanks to the short distance between the particles in the region of interest. Sodium could be detected on the nanoparticle surfaces, suggesting that the method can be used to study ligands or adsorbents that are used in solution on particles.

However, the attempts to attach thiol modified proteins to the nanoparticles and study them by APT was so far not successful. This can be explained by the low degree of binding of streptavidin and biotin modified gold nanoparticle complexes to the surface-bound nanoparticles, as observed in TEM. Furthermore, the apparent poor adhesion between silica and the gold nanoparticles caused micro-fractures in the specimen during analysis when the voltage was applied, which could explain the observed results where the particles appear to be surrounded by chromia rather than silica. Further work is required to improve the adhesion of the silica layer to more reliably be able to study the ligands of the nanoparticles in their hydrated state.

Further work is also required to reliably be able to bind biomolecule ligands to the nanoparticles prior to silica embedding, which could allow for APT analysis of such molecules in a reproducible way using conventional sample preparation methods. Recent development in APT instrumentation could also allow for a higher success rate in analysis of these materials. For example, the use of shorter wavelength lasers, in the UV-range, could improve the thermal activation of field evaporation, reducing the risk of specimen fracture.

The analysis of bone-like hydroxyapatite nanoparticles on titanium surfaces showed the immobilization mechanism by integration of calcium and phosphorous into the titanium oxide layer, contributing to the understanding of the improved performance of this type of material as medical devices. In order to enable investigation of the surface coating and oxide, the material was sputter coated with a protective chromium layer to provide a matrix for the nanoparticles as well as enabling APT specimen preparation with conventional FIB-SEM

protocols. The material proved to run well during APT analysis conditions, despite several interfaces that could be weak points. However, the tendency of chromium to oxidize and the titanium oxide caused a large number of peaks in the mass spectrum, making quantitative analysis of the calcium and phosphate content challenging.

Compared to EDX results by HAADF-STEM, the measured content in the APT reconstructions was lower, due to overlaps in the mass spectrum. Still, APT data confirmed the presence of calcium and phosphate throughout the entire titanium oxide layer with a higher resolution than EDX. Future studies on similar materials could be conducted on titanium implants coated with hydroxyapatite nanoparticle after being used *in vivo*. This could provide insight in differences in osseointegration of such materials compared to conventional titanium implants without any surface modification. It could also be of interest to compare the calcium and phosphorous content in the titanium oxide layer of a modified titanium surface before and after osseointegration.

6. Acknowledgements

7. References

1. Lundstrom K. Structural genomics for membrane proteins. Cell Mol Life Sci. 2006;63(22):2597–607.

2. Miller MK. Atom probe tomography and the local electrode atom probe. Vol. 10, Microscopy and Microanalysis. 2004. 150–151 p.

3. Kelly TF, Nishikawa O, Panitz JA, Prosa TJ. Prospects for nanobiology with atom-probe tomography. MRS Bull. 2009;34(10):744–9.

4. Sundell G, Hulander M, Pihl A, Andersson M. Atom Probe Tomography for 3D Structural and Chemical Analysis of Individual Proteins. Small. 2019;15(24):1–6.

5. Crick F. Central Dogma of Molecular Biology. Nature. 1970;227:561–3.

6. Brooks-Bartlett JC, Garman EF. The nobel science: One hundred years of crystallography. Interdiscip Sci Rev. 2015;40(3):244–64.

7. Ealias AM, Saravanakumar MP. A review on the classification, characterisation, synthesis of nanoparticles and their application. IOP Conf Ser Mater Sci Eng. 2017;263(3).

8. Herizchi R, Abbasi E, Milani M, Akbarzadeh A. Current methods for synthesis of gold nanoparticles. Artif Cells, Nanomedicine Biotechnol. 2016;44(2):596–602.

9. Kumar D, Meenan BJ, Mutreja I, D'Sa R, Dixon D. Controlling the size and size distribution of gold nanoparticles: A design of experiment study. Int J Nanosci. 2012;11(2).

10. Zhao P, Li N, Astruc D. State of the art in gold nanoparticle synthesis. Coord Chem Rev. 2013;257(3–4):638–65.

11. Personick ML, Langille MR, Zhang J, Mirkin CA. Shape control of gold nanoparticles by silver underpotential deposition. Nano Lett. 2011;11(8):3394–8.

12. Grzelczak M, Pérez-Juste J, Mulvaney P, Liz-Marzán LM. Shape control in gold nanoparticle synthesis. Chem Soc Rev. 2008;37(9):1783–91.

13. Hsieh S, Chao WJ, Hsieh CW. Improved performance of aminopropylsilatrane over aminopropyltriethoxysilane as an adhesive film for anchoring gold nanoparticles on silicon surfaces. J Nanosci Nanotechnol. 2009;9(5):2894–901.

14. Chen WH, Tseng YT, Hsieh S, Liu WC, Hsieh CW, Wu CW, et al. Silanization of solid surfaces via mercaptopropylsilatrane: A new approach of constructing gold colloid monolayers. RSC Adv. 2014;4(87):46527–35.

15. Mendes BB, Conniot J, Avital A, Yao D, Jiang X, Zhou X, et al. Nanodelivery of nucleic acids. Nat Rev Methods Prim. 2022;2(1).

16. Dobrovolskaia MA, McNeil SE. Immunological properties of engineered nanomaterials: An introduction. Handb Immunol Prop Eng Nanomater Second Ed. 2016;1:1–24.

17. Avvakumova S, Colombo M, Galbiati E, Mazzucchelli S, Rotem R, Prosperi D. Bioengineered Approaches for Site Orientation of Peptide-Based Ligands of Nanomaterials. In: Biomedical Applications of Functionalized Nanomaterials: Concepts, Development and Clinical Translation. Elsevier Inc.; 2018. p. 139–69.

18. Avvakumova S, Colombo M, Tortora P, Prosperi D. Biotechnological approaches toward nanoparticle biofunctionalization. Trends Biotechnol. 2014;32(1):11–20.

19. Frasconi M, Mazzei F, Ferri T. Protein immobilization at gold-thiol surfaces and potential for biosensing. Anal Bioanal Chem. 2010;398(4):1545–64.

20. Aslan K, Luhrs CC, Pérez-Luna VH. Controlled and reversible aggregation of biotinylated gold nanoparticles with streptavidin. J Phys Chem B. 2004;108(40):15631–9.

21. Hou X, Zaks T, Langer R, Dong Y. Lipid nanoparticles for mRNA delivery. Nat Rev Mater. 2021;6(12):1078–94.

22. Westas E, Gillstedt M, Lönn-Stensrud J, Bruzell E, Andersson M. Biofilm formation on nanostructured hydroxyapatite-coated titanium. J Biomed Mater Res - Part A. 2014;102(4):1063–70.

23. Suchanek W, Yoshimura M. Processing and properties of hydroxyapatite-based biomaterials for use as hard tissue replacement implants. J Mater Res. 1998;13(1):94–117.

24. LeGeros RZ. Calcium phosphate-based osteoinductive materials. Chem Rev. 2008;108(11):4742–53.

25. Anderson RS, Anderson SP. Geomorphology: The Mechanics and Chemistry of Landscapes. Cambridge University Press; 2010. 187 p.

26. Hans Wedepohl K. The composition of the continental crust. Geochim Cosmochim Acta. 1995;59(7):1217–32.

27. Ravindra R, Zhao S, Gies H, Winter R. Protein encapsulation in mesoporous silicate: The effects of confinement on protein stability, hydration, and volumetric properties. J Am Chem Soc. 2004;126(39):12224–5.

28. Stöber W, Fink A, Bohn E. Controlled Growth of Monodisperse Silica Spheres in the Micron Size Range. J Colloid Interface Sci. 1968;26(1):62–9.

29. Bogush GH, Tracy MA, Zukoski CF. Preparation of monodisperse silica particles: Control of size and mass fraction. J Non Cryst Solids. 1988;104(1):95–106.

30. Bhatia RB, Brinker CJ, Gupta AK, Singh AK. Aqueous sol-gel process for protein encapsulation. Chem Mater. 2000;12(8):2434–41.

31. Belton DJ, Deschaume O, Perry CC. An overview of the fundamentals of the chemistry of silica with relevance to biosilicification and technological advances. FEBS J. 2012;279(10):1710–20.

32. Liu DM, Chen IW. Encapsulation of protein molecules in transparent porous silica matrices via an aqueous colloidal sol-gel process. Acta Mater. 1999;47(18):4535–44.

33. Brinker CJ, Hurd AJ, Schunk PR, Frye GC, Ashley CS. Review of sol-gel thin film formation. J Non Cryst Solids. 1992;147–148(C):424–36.

34. Williams DB, Carter CB. Tranmission Electron Microscopy. Second edi. New York: Springer Science+Business Media; 2009.

35. Goldstein JI, Newbury DE, Michael JR, Ritchie NWM, Scott JHJ, Joy DC. Scanning Electron Microscopy and X-Ray Microanalysis. Fourth edi. New York: Springer Science+Business Media; 2018.

36. Giannuzzi LA, Stevie FA. Introduction to Focused Ion Beams: Instrumentation, Theory, Techniques and Practice. First Edit. New York: Springer Science+Business Media; 2005.

37. Giannuzzi LA, Michael JR. Comparison of Channeling Contrast between Ion and Electron Images. Microsc Microanal. 2013 Apr [cited 2022 Oct 5];19(2):344–9.

38. Giannuzzi LA, Stevie FA. A review of focused ion beam milling techniques for TEM specimen preparation. Micron. 1999;30(3):197–204.

39. Langford RM, Clinton C. In situ lift-out using a FIB-SEM system. Micron. 2004;35(7):607–11.

40. Mayer J, Giannuzzi LA, Kamino T, Michael J. TEM Sample Preparation and FIB-Induced Damage. MRS Bull. 2007;32(May):400–7.

41. Lefebvre-Ulrikson W, Vurpillot F, Sauvage X. Atom Probe Tomography: Put Theory Into Practice. Edition 1st, editor. Academic Press; 2016.

42. Gault B, Chiaramonti A, Cojocaru-Mirédin O, Stender P, Dubosq R, Freysoldt C, et al. Atom probe tomography. Nat Rev Methods Prim. 2021;1(1).

43. Hatzoglou C, Rouland S, Radiguet B, Etienne A, Costa G Da, Sauvage X, et al. Preferential Evaporation in Atom Probe Tomography: An Analytical Approach. Microsc Microanal. 2020;26(4):689–98.

44. Melmed AJ. The art and science and other aspects of making sharp tips. J Vac Sci Technol B Microelectron Nanom Struct. 1991;9(2):601.

45. Thompson K, Lawrence D, Larson DJ, Olson JD, Kelly TF, Gorman B. In situ site-specific specimen preparation for atom probe tomography. Ultramicroscopy. 2007;107(2–3):131–9.

46. Larson DJ, Prosa TJ, Ulfig RM, Geiser BP, Kelly TF. Data Processing and Reconstruction. In: Local Electrode Atom Probe Tomography. New York: Springer Science+Business Media; 2013. p. 109–62.

47. Park YK, Park S. Directing close-packing of midnanosized gold nanoparticles at a water/hexane interface. Chem Mater. 2008;20(6):2388–93.

48. Hernández-Saz J, Herrera M, Molina SI. A methodology for the fabrication by FIB of needle-shape specimens around sub-surface features at the nanometre scale. Micron. 2012;43(5):643–50.

49. Kempshall BW, Giannuzzi LA, Prenitzer BI, Stevie FA, Da SX. Comparative evaluation of protective coatings and focused ion beam chemical vapor deposition processes. J Vac Sci Technol B Microelectron Nanom Struct. 2002;20(1):286.

50. Bunton JH, Olson JD, Lenz DR, Kelly TF. Advances in pulsed-laser atom probe: Instrument and specimen design for optimum performance. Microsc Microanal. 2007;13(6):418–27.

51. Kuzuya A, Numajiri K, Kimura M, Komiyama M. Single-Molecule Accommodation of Streptavidin in Nanometer-Scale Wells Formed in DNA Nanostructures. Nucleic Acids Symp Ser. 2008 Sep 1;52(1):681–2.

52. Jun H, Jang K, Jung C, Choi PP. Atom Probe Tomography Investigations of Ag Nanoparticles Embedded in Pulse-Electrodeposited Ni Films. Microsc Microanal. 2021;27(5):1007–16.

53. La Fontaine A, Yen HW, Felfer PJ, Ringer SP, Cairney JM. Atom probe study of chromium oxide spinels formed during intergranular corrosion. Scr Mater. 2015;99:1–4.

54. Tsong TT. Field ion image formation. Surf Sci. 1978 Jan 1;70(1):211–33.

55. Landi E, Celotti G, Logroscino G, Tampieri A. Carbonated hydroxyapatite as bone substitute. J Eur Ceram Soc. 2003;23(15):2931–7.

56. Mosiman DS, Chen YS, Yang L, Hawkett B, Ringer SP, Mariñas BJ, et al. Atom Probe Tomography of Encapsulated Hydroxyapatite Nanoparticles. Small Methods. 2021;5(2):1–8.

57. Langelier B, Wang X, Grandfield K. Atomic scale chemical tomography of human bone. Sci Rep. 2017;7(January):1–9.

58. Karlsson J, Sundell G, Thuvander M, Andersson M. Atomically resolved tissue integration. Nano Lett. 2014;14(8):4220–3.

59. Sundell G, Dahlin C, Andersson M, Thuvander M. The bone-implant interface of dental implants in humans on the atomic scale. Vol. 48, Acta Biomaterialia. 2017. p. 445–50.